Diplomarbeit

submitted to the
Institute of Theoretical Physics
Of the Technical University of Vienna, Austria

for the degree of
Dipl.-Ing.

Put forward by
Tobias Angelli

Examined and approved on

____

by the following examiner:

____

Priv.-Doz. Dr.rer.nat. Kirill Boguslavski (Betreuer)

Eidesstaatliche Erklärung

Ich erkläre an Eides statt, dass die vorliegende Arbeit nach den anerkannten Grundsätzen für wissenschaftliche Abhandlungen von mir selbstständig erstellt wurde. Alle verwendeten Hilfsmittel, insbesondere die zugrunde gelegte Literatur, sind in dieser Arbeit genannt und aufgelistet. Die aus den Quellen wörtlich entnommenen Stellen, sind als solche kenntlich gemacht. Das Thema dieser Arbeit wurde von mir bisher weder im In- noch Ausland einer einem Beurteiler zur Begutachtung in irgendeiner Form als Prüfungsarbeit vorgelegt. Diese Arbeit stimmt mit der von den Begutachtern beurteilten Arbeit überein.

Ort, Datum

....
(Tobias Angelli)

Spectral functions in a Bjorken expanding space-time

Zusammenfassung

Wir erörtern die physikalischen Eigenschaften von $O(N)$-symmetrischen relativistischen Skalarfeldtheorien in einer Bjorken-expandierenden Hintergrundgeometrie. Diese geometrische Struktur wird auf Grund der abgebildeten longitudinalen Expansion besonders häufig zum Studium von Schwerionenkollisionen herangezogen. Indem wir klassisch-statistische Gittersimulationen anwenden, können wir Korrelationsfunktionen berechnen, welche Einsicht in die reichhaltige Struktur der Moden- und Quasiteilchenanregungen bietet. Zur Einstimmung auf die wechselwirkende Theorie werden vor allem Spektralfunktionen der freien Theorie in der longitudinal-expandierenden Geometrie betrachtet. Anschließend — vermittels der selben numerischen Technik — extrahieren wir Nichtgleichzeitigkeitskorrelatoren aus dem wechselwirkenden Modell. Die Fourier-transformierten Korrelatoren zeigen einen einzigen Peak, den wir zur Bestimmung der Dämpfungsrate und der Dispersionsrelation heranziehen. Weiters erfüllen sie die verallgemeinerte Fluktuations-Dissipations-Beziehung. Damit stellen wir fest, dass die Anregungen unterschiedlich ausfallen als im nichtexpandierenden Minkowski-Hintergrund. Im Speziellen erkennt man, dass wir unterschiedliche Arten von Anregungen sehen, welche vom transversalen bzw. longitudinalen Impuls abhängen. Wir versuchen die Ursache dieses Verhaltens mit den Eigenschaften der Bjorken-Expansion zu erläutern, allen voran der damit assoziierten Rotverschiebung. In Zukunft könnte man diese Anregungen mit jenen aus Eichtheorien in einer expandierenden Geometrie vergleichen.

Abstract

We examine the physical properties of an $O(N)$-relativistic scalar field theory in a Bjorken-expanding geometry, i.e. a longitudinally expanding metric tensor that is frequently used to address heavy-ion collisions. Employing classical statistical lattice simulations, we extract correlation functions that provide insight into a rich structure concerning mode occupancies and quasiparticle peaks. Firstly, an investigation in the noninteracting version of the theory is performed to learn key features of spectral functions in the expanding geometry. The same techniques to analyze the data are then employed to study unequal-time correlation functions obtained in the interacting theory. In particular, we define spectral and statistical functions and compute them independently. We find that they are related by a generalized fluctuation-dissipation relation. For each momentum, they display a single excitation peak in frequency space of which we extract the dispersion relation and damping rate. We observe that this peak shows a fundamental difference between transverse and longitudinal momentum modes while showing a mixture of their properties for other momenta. We argue that these properties can be attributed to features in the Bjorken-expanding geometry like dilution and longitudinal redshift that are already present in the free theory. We find that the excitations are of a fundamentally different nature as compared to a non-expanding Minkowski background. Thus, we determined the excitation spectrum of a scalar theory in an expanding background. Future research might focus on gauge theories in a Bjorken-expanding geometry and compare them for different far-from-equilibrium universality classes that may show structural similarities in their excitation peaks but differ in a more detailed comparison.

Contents

Chapter 1

Introduction

A path to understanding physical phenomena in thermal quantum field theories is to study the nature of the universality classes of said systems. Such cases of universality are usually associated with observations in statistical mechanics, namely that macroscopic properties are independent of the microscopical details of a system. This opens the possibility to group multiple different systems together by considering only their shared dynamical behavior, while simultaneously ignoring the messy microscopic properties. These groups — called universality classes — allow us to study complex physical systems by using the simplest representative of the class. In the historical context, this was usually done to examine critical points in or near thermal equilibrium [1].

In stark contrast, we focus on systems that are far away from thermal equilibrium, thereby exhibiting unusually large occupancies per mode. Conceptionally, there are some similarities between nonequilibrium and close-to-equilibrium systems: In the latter case, if the system undergoes a phase transition, the correlation functions show a self-similar evolution, i.e. regardless of our resolution of the microscopic details, the correlation functions look the same, being solely described by a universal scaling function f and a critical exponent ζ. In the case of a far-from-equilibrium system, we detect that the system approaches a nonthermal fixed point. In the vicinity of such points, the correlation functions of the system become independent of the scale leading to a sufficient description by a universal scaling function f and two universal exponents α and β[2]. A remarkable feature is that this behavior occurs at the opposite points of the energy scale: Namely at the high-energy end in early inflation models of cosmology and heavy-ion collisions, and in total contrast to the former, in ultracold Bose gases [3–11]. Moreover, the existence of nonthermal fixed points in the latter case was experimentally verified [12–18].

Our major focus resides on the far-from-equilibrium dynamics in heavy-ion collisions in the ultrarelativistic limit. Such collisions are extensively studied in experiments carried out at the Large Hadron Collider at CERN, Switzerland and at the Relativistic Heavy Ion Collider at the Brookhaven National Lab in the United States. In both facilities, the nuclei of heavy elements — especially lead — are accelerated to extremely high energies before colliding with each other. The relevant forces under these circumstances are governed by the laws of quantum chromodynamics (QCD), which describes the strong nuclear force, one of the four fundamental interactions in the standard model. The resulting state of matter from these collisions is called the Quark-Gluon Plasma (QGP). Although this state is usually described by QCD [19–21], we simplify the mathematical structure by choosing relativistic scalar fields. This is motivated by an intermediate momentum regime, where the dynamics of the particle distribution of scalar fields have been shown to follow the same evolution as in Yang-Mills-theories (YM-theories) [3, 5]. Our particular aim is to determine the nature of the nonequal-time correlators, namely the spectral function ρ and the statistical correlator F since both encode the structure of the excitation spectrum.

In this thesis, our model is an isolated quantum many-body system [22] consisting of scalar constituents, whose interaction is described by a φ^4-potential. The scalars are taken to follow an $O(N)$-symmetry and to live in a longitudinally expanding background geometry that mimics the situation in heavy-ion collisions [23]. While the relevant interaction is described by quantum chromodynamics, a nonabelian gauge theory, our scalar model has been argued to possess a universal momentum region that shows the same dynamical scaling behavior as non-abelian plasmas [3]. In particular, we make the first crucial step towards scrutinizing this conjectured universality. We study the excitation spectrum of the expanding scalar theory to learn about the quasiparticle properties in a longitudinally expanding background metric.

Methodologically, we conduct classical statistical lattice simulations. This approximation is justified due to the large occupation number of the system that allows us to omit quantum fluctuations in the action functional and to solely focus on the classical dynamical evolution of the fields [24, 25]. The approach is often applied in far-from-equilibrium systems, although increasingly effective kinetic theories might be used to examine the dynamics near nonthermal fixed points in many-body quantum systems [26–30] or the study of renormalization group flows and 2PI methods [31–35]. The main focus of this work is using a real-time lattice to extract a series of equal and unequal time correlators. In order to extract the latter type of correlation function, we use an approach from linear response theory, which is necessary to extract the spectral function from our simulation. The usage of linear fluctuations to perturb our system and the subsequent study of spectral functions in order to obtain the excitation spectrum of complex quantum systems is well established by the scientific literature [36–48]. The simulation code is implemented in C++ and was modified to allow for the extraction of the correlators in an expanding background. At late times, we encountered problems with the signal resolution. These issues are discussed in appendix B. However, the thesis focuses on the successful computation of the correlators at earlier times.

The main points of this thesis can be summarized as follows:

- The reproduction of previously established results regarding equal time correlators and the scaling exponents of the universality class.

- The calculation of the spectral function and the statistical correlator for different modes, depending on the values of transversal momentum p_T and rapidity ν.

This is the first computation of such unequal-time correlation functions in a longitudinally expanding background for scalar quantum many-body systems.

Outline

The thesis is outlined as follows: In section 2, we give an overview of the theoretical background regarding relativistic scalar field theory for a generally time-dependent diagonal metric tensor. Then we will focus our attention on the explanation and introduction of Bjorken coordinates before we describe the numerical technique. In chapter 3, a brief summary of scalar field theory in a flat background is provided. In this chapter, we will introduce the concept of universality classes, which we will describe according to the scaling properties of the distribution function $f(p,t)$. We conclude this section with an examination of the spectral function and the statistical correlator. The last two chapters, 4 and 5, are dedicated to the expanding scalar system. In section 4, we will discuss the properties of different mode functions when the interaction is turned off. Finally, we will describe the intermediate momentum universality class and the dispersion relation $\omega(p_T, \nu, \tau)$ before we compare the unequal time excitations (in time and frequency space) of the interacting theory in chapter 5. We summarize our results in chapter 6. In the appendices, we give an overview of the numerical Fourier transformation and we describe the difficulties that arose from late-time simulations.

Conventions

We chose natural units where the speed of light c and Planck's constant $\hbar$ are set to 1. This is in accordance with the conventions in high energy physics, where it is convenient to express physical measurements in units of GeV.

The spacetime metric follows the mostly-minus convention, where the "temporal" entry is prefixed by a plus sign and the spatial entries by minus:

$$\eta_{\mu\nu} = \begin{pmatrix} 1 & 0 & 0 & 0 \\ 0 & -1 & 0 & 0 \\ 0 & 0 & -1 & 0 \\ 0 & 0 & 0 & -1 \end{pmatrix}.$$

We denote 4-vectors using Greek indices and boldface letters to denote 3-vectors. In accordance with our metric convention, the scalar product of two 4-vectors is

$$p^2 = p^\mu p_\mu = (p^0 p_0) - |\mathbf{p}|^2.$$

Latin indices are used as color indices. Note that — differently from the Lorentz indices from above — their position is irrelevant, i.e. we can raise or lower them as it is convenient:

$$\psi_a = \psi^a \equiv \delta^{ab}\psi_b.$$

Chapter 2

Theoretical considerations

The quantum theory of scalar fields is oftentimes regarded as a toy model of the real world compared to gauge theories. Accordingly, the mathematical structure of the former, while rightly believed to be simpler, contains nevertheless a rich set of possibilities to dive into physical phenomena, like early inflation models of the universe or ultracold Bose gases.

In this section of the thesis, we concern ourselves with the mathematical structure of a scalar field theory with an $O(N)$-symmetry in a general background geometry. We will describe the definition of the field operators and correlators derived from a generating functional, and introduce the statistical and spectral functions.

Afterward, we will provide a motivation for the introduction of Bjorken coordinates. In this context, a physical explanation of proper time and rapidity is given with regard to special relativity.

A justification for the usage of a classical statistical lattice simulation is relegated to section 2.2, where we will discuss the ideas behind the numerical technique whose applicability for scalar, gauge and Yang-Mills theories is well established by literature (vid. [5, 49, 50]).

2.1 The scalar field theory

The canonical way to arrive at a description of a quantum field theory is via the path integral formalism. In this section, we will derive the action for a relativistic $O(N)$ scalar field theory in a background geometry defined by the metric tensor $g_{\mu\nu}$. After defining the fields and their conjugate momenta, we will summarize the nonequilibrium structure of the theory. Lastly, a short motivation for the introduction of Bjorken coordinates and their meaning in the context of quantum field theory is provided.

2.1.1 Action and fields of the scalar theory

The dynamics of free scalar fields are governed by the Klein-Gordon equation

$$(\partial_\mu \partial^\mu + m^2)\phi = 0. \tag{2.1}$$

For an interacting theory, we will provide the most elemental modification for the Lagrangian density $\mathcal{L}$ by adding a φ^4 anharmonic potential term to it. $\mathcal{L}$ is constructed such that it satisfies an $O(N)$-symmetry, i.e. we have to consider N scalar fields[1]. Thus the action takes on the form

$$S[\varphi] = \int d^4x \sqrt{-g} \left(\frac{1}{2} g^{\mu\nu} \partial_\mu \varphi_a \partial_\nu \varphi_a - \frac{1}{2} m^2 \varphi_a \varphi_a - \frac{\lambda}{4! N} (\varphi_a \varphi_a)^2 \right), \tag{2.2}$$

where it is clearly seen that the dynamical effects of the geometry reside in the first term and in the factor $\sqrt{-g}$, the square root of the determinant of the metric, that is the result of the coordinate transformation. For the sake of brevity, we will set the mass m to zero and perform the following calculations on the massless action. Our assumption is justified since the universality was only observed between massless scalars and gauge plasmas in [3, 23].

To derive the equation of motions for the fields φ_a, we will calculate the variation of the action:

$$\frac{\delta S[\varphi]}{\delta \varphi_b} = 0.$$

Since the calculation is — in part due to the general background — quite involved, we will simplify it via the usage of the Christoffel symbol that is defined as

$$\Gamma^\rho{}_{\mu\nu} = \frac{1}{2} g^{\rho\sigma} \left(\partial_\nu g_{\sigma\mu} + \partial_\mu g_{\sigma\nu} - \partial_\sigma g_{\mu\nu} \right).$$

[1] Latin indices mark the different scalar fields while greek indices are Lorentz indices.

We employ the formula $\Gamma^{\rho}{}_{\mu\rho} = \partial_\mu \ln \sqrt{-g}$ in the following calculation:

$$\begin{aligned}
\frac{\delta S}{\delta \varphi_b} &= -\partial_\mu \left(\sqrt{-g} g^{\mu\nu} \partial_\nu \varphi_b\right) - \sqrt{-g}\frac{\lambda}{3!N}(\varphi_a\varphi_a)\varphi_b \\
&= -\frac{\sqrt{-g}}{\sqrt{-g}}\partial_\mu\sqrt{-g} g^{\mu\nu}\partial_\nu\varphi_b - \sqrt{-g}\partial_\mu g^{\mu\nu}\partial_\nu\varphi_b - \sqrt{-g}g^{\mu\nu}\partial_\mu\partial_\nu\varphi_b - \sqrt{-g}\frac{\lambda}{3!N}(\varphi_a\varphi_a)\varphi_b \\
&= -\sqrt{-g}\left(\Gamma^{\rho}{}_{\mu\rho}g^{\mu\nu}\partial_\nu + \partial_\mu g^{\mu\nu}\partial_\nu + g^{\mu\nu}\partial_\mu\partial_\nu + \frac{\lambda}{3!N}(\varphi_a\varphi_a)\right)\varphi_b \\
&= 0
\end{aligned}$$

Finally, the equation of motion of the φ^4-theory reads

$$\left(\Gamma^{\rho}{}_{\mu\rho}g^{\mu\nu}\partial_\nu + \partial_\mu g^{\mu\nu}\partial_\nu + g^{\mu\nu}\partial_\mu\partial_\nu + \frac{\lambda}{3!N}(\varphi_a\varphi_a)\right)\varphi_b = 0. \tag{2.3}$$

We will put two constraints on the metric tensor for the following calculations: $g_{\mu\nu}$ shall be diagonal and it will only depend on x^0, i.e. we will assume $g^{00} = 1$. Using the Lagrangian density from (2.2), it is possible to derive the Hamiltonian density $\mathcal{H}$ by introducing the canonically conjugate momentum field π_a as

$$\pi_b = \frac{\delta S}{\delta \partial_0 \phi_b},$$

followed by a Legendre transformation, resulting in

$$\mathcal{H} = \sqrt{-g}\left(\frac{1}{2}\pi_a\pi_a + \frac{1}{2}g^{ij}\partial_i\varphi_a\partial_j\varphi_a + \frac{\lambda}{4!N}(\varphi_a\varphi_a)^2\right).$$

The first order differential equations derived from $\mathcal{H}$ are

$$\partial_0\pi_a = -\frac{\delta\mathcal{H}}{\delta\varphi_a} = -g^{ij}\partial_i\partial_j\varphi_a - \frac{\lambda}{3!N}(\varphi_b\varphi_b)\varphi_a \qquad \text{and} \qquad \partial_0\phi_a = \frac{\delta\mathcal{H}}{\delta\pi_a} = \sqrt{-g}\pi_a. \tag{2.4}$$

Now we shall leave the realm of classical fields and enter the world of quantum mechanics. To this end I will introduce the Heisenberg field operators Φ_a and Π_a via the canonical commutation relations:

$$[\Phi_a(x^\mu), \Pi_b(\tilde{x}^\mu)] = \mathrm{i}\delta_{ab}\delta(x^\mu - \tilde{x}^\mu), \tag{2.5}$$

$$[\Phi_a(x^\mu), \Phi_b(\tilde{x}^\mu)] = 0, \tag{2.6}$$

$$[\Pi_a(x^\mu), \Pi_b(\tilde{x}^\mu)] = 0. \tag{2.7}$$

Using the creation and annihilation operators $a^\dagger, a$, one can perform a »plane wave« expansion. The possibility of an expanding background engenders a special attentiveness with regard to the actual waves.

In a flat Minkowski geometry, so-called mode functions $\xi_p(t)$ are introduced as solutions to the spatially Fourier-transformed Klein-Gordon-equation

$$\partial_t^2 \xi_p(t) + (p^k p_k + m^2)\xi_p(t) = 0, \tag{2.8}$$

whose form are $\xi_p(t) \propto e^{\mathrm{i}\omega_p t}$ with $\omega_p = \sqrt{p^2 + m^2}$. The above equation changes to (2.3) — provided the coupling λ is set to zero — in a general background geometry, and so does the resulting dispersion relation ω and the mode function $\xi(t)$. Nevertheless, we can express the field and its conjugate momenta as Fourier transformation of the creation and annihilation operators and their associated mode function:

$$\Phi_b \sim \int \frac{d^3\tilde{p}}{(2\pi)^3} \left(a_b(\tilde{p})\xi_{\mathbf{p}}(t)e^{\mathrm{i}\tilde{p}x} + a_b^\dagger(\tilde{p})\xi_{\mathbf{p}}^*(t)e^{-\mathrm{i}\tilde{p}x} \right), \tag{2.9}$$

$$\Pi_b \sim \sqrt{-g} \int \frac{d^3\tilde{p}}{(2\pi)^3} \left(a_b(\tilde{p})\partial_0\xi_{\mathbf{p}}(t)e^{\mathrm{i}\tilde{p}x} + a_b^\dagger(\tilde{p})\partial_0\xi_{\mathbf{p}}^*(t)e^{-\mathrm{i}\tilde{p}x} \right). \tag{2.10}$$

The annihilation operator becomes

$$a_{b,\mathbf{p}}(x^0) = \mathrm{i}\sqrt{-g(x^0)} \int d^3x \left(\xi_{\mathbf{p}}^*(x^0) \overleftrightarrow{\partial_0} (\Phi_b(\mathbf{x}, x^0) - \phi_b(x^0)) \right) e^{-\mathrm{i}\mathbf{p}\mathbf{x}}, \tag{2.11}$$

where we used $f \overleftrightarrow{\partial} g = f\partial g - \partial f g$. The creation operator $a^\dagger$ is obtained by taking the Hermitian conjugate of equation 2.11. The definition of the operators forces the mode functions $\xi_{\mathbf{p}}$ to satisfy the conditions $(\partial_0 \xi_{\mathbf{p}})^* = \partial_0 \xi_{\mathbf{p}}^*$ and $\xi_{\mathbf{p}} \overleftrightarrow{\partial_0} \xi_{\mathbf{p}}^* = \mathrm{i}/\sqrt{-g}$.

2.1.2 Nonequilibrium quantum field theory

In this part of my work, we intend to give a short overview of nonequilibrium quantum field theory primarily based on [51].

A quantum system is — following the »statistical« interpretation of quantum mechanics (vid. [52]) — fully described by its density operator $\rho(t)$, whose time evolution is given in analogy to the classical Liouville equation[2] by the von Neumann equation

$$\partial_t \rho(t) = -\mathrm{i}[H(t), \rho(t)]. \tag{2.12}$$

But, in accordance with the Schrödinger picture, the time evolution of a quantum state is determined by applying the unitary operator

$$U(t, t') = T \exp\left(-\mathrm{i} \int_{t'}^{t} dt'' H(t'')\right)$$

to the density operator as follows:

$$\rho(t) = U(t, t_0)\rho(t_0)U(t_0, t).$$

For the statistical interpretation to make sense, we require the normalization condition $\mathrm{tr}(\rho(t)) = 1$. Finally, the expectation value of a general physical observable $\mathcal{O}$ is given by

$$\langle \mathcal{O} \rangle(t) = \mathrm{tr}(\rho(t)\mathcal{O}) \tag{2.13}$$

$$= \mathrm{tr}\left(\rho_0 U(t_0, t)\mathcal{O}U(t, t_0)\right). \tag{2.14}$$

By a mathematical sleight of hand, we move to the Heisenberg picture of quantum mechanics and give a different explanation. If time evolution happens in the operator, not in the states, the interval $[t_0, t]$ might be partitioned into equidistant subintervals of length δt as in figure 2.1. Thus it becomes possible to write down a generating functional that depends on two sources J_a and R_{ab}:

$$Z[J, R] = \mathrm{tr}\left[\rho_0 T_{\mathcal{C}} \exp\left(\mathrm{i}\left(\int_{\mathcal{C}} d^4x J_a(x)\Phi_a(x) + \frac{1}{2}\int_{\mathcal{C}} d^4x d^4y R_{ab}(x, y)\Phi_a(x)\Phi_b(y)\right)\right)\right]. \tag{2.15}$$

Time ordering along the contour $\mathcal{C}$ is dictated by the operator $T_{\mathcal{C}}$ in a way such that times on the negative contour $\mathcal{C}^-$ are always »later« compared to the ones on $\mathcal{C}^+$. A salient feature of

[2]The classical Liouville equation $\dot{\rho} = -\{\rho, H\}$ goes over to the von Neumann equation by replacing the Poisson bracket $\{\cdot, \cdot\}$ with the commutator $[\cdot, \cdot]$.

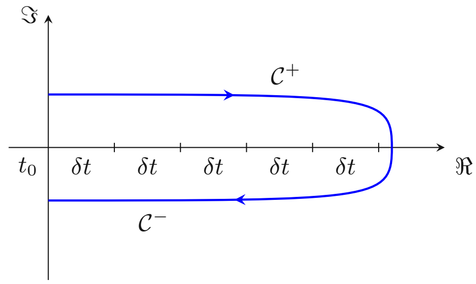

Figure 2.1: Conceptional drawing of the Schwinger-Keldysh time contour ([53]) in the Gauß plane. The δt refers to small time steps.

(2.15) is the possibility to derive n-point correlators using functional derivatives:

$$-\frac{\mathrm{i}}{\sqrt{-g}}\frac{\delta Z}{\delta J_a} = \langle \Phi_a \rangle = \phi_a, \qquad \frac{\mathrm{i}}{\sqrt{-g}}\frac{\mathrm{i}}{\sqrt{-g}}\frac{\delta^2 Z}{\delta J_a \delta J_b} = \langle T_{\mathcal{C}} \Phi_a(x)\Phi_b(y)\rangle = G_{ab}(x,y) + \phi_a\phi_b. \tag{2.16}$$

All further correlation functions result from the application of Wick's theorem (vid. [53]). We use the two-point correlators from equation (2.16) to build the statistical correlator and the spectral function as anticommutator and commutator of the respective two-point correlation function:

$$F_{ab}(x^\mu, y^\nu) = \frac{1}{2}\langle\{\Phi_a(x^\mu), \Phi_b(y^\nu)\}\rangle - \phi_a(x^\mu)\phi_b(y^\nu), \qquad \rho_{ab}(x^\mu, y^\nu) = \mathrm{i}\langle[\Phi_a(x^\mu), \Phi_b(y^\nu)]\rangle. \tag{2.17}$$

It seems supererogatory to mention that F_{ab} is symmetric and ρ_{ab} is antisymmetric under the exchange of their arguments since it is a direct consequence of their algebraic definitions. Physically, the statistical correlator determines, how often states are occupied, while the spectral function enables us to study the excitation structure of the field theory. This is in some ways similar to the Lehmann-Källén form of the exact propagator in vacuum quantum field theory [54].

If the system reaches thermal equilibrium, F and ρ are no longer independent but related by the Kubo-Martin-Schwinger condition (KMS), otherwise known as the fluctuation-dissipation relation:

$$F(p^0, \mathbf{p}, t) = -\mathrm{i}\left(f(p^0, \mathbf{p}, t) + \frac{1}{2}\right)\rho(p^0, \mathbf{p}, t). \tag{2.18}$$

The KMS condition fixes the single-particle distribution function $f(p^0, \mathbf{p}, t)$ to the well-known Bose-Einstein distribution function, hence destroying the out-of-equilibrium-independence of

F and ρ.

The symmetry of the statistical correlator allows us to calculate it at equal times. Thus we arrive at the possibility of defining the function F (and its time derivatives) that is related to the distribution of quasiparticles in the system:

$$F(\mathbf{p},t) = \frac{1}{N} F_{aa}(x^0,\mathbf{p},x^0), \tag{2.19}$$

$$\ddot{F}(\mathbf{p},t) = \sqrt{-g(x^0)}\sqrt{-g(\tilde{x}^0)}\partial_0\partial_{\tilde{0}} F(\mathbf{p},x^0,\tilde{x}^0)\Big|_{x^0=\tilde{x}^0}. \tag{2.20}$$

$$\dot{F}(\mathbf{p},t) = \frac{1}{2}\left(\sqrt{-g(x^0)}\partial_0 + \sqrt{-g(\tilde{x}^0)}\partial_{\tilde{0}}\right) F(\mathbf{p},x^0,\tilde{x}^0)\Big|_{x^0=\tilde{x}^0}. \tag{2.21}$$

The general nonequilibrium distribution function is calculated from the time-derivatives of the equal-time correlator F:

$$f(\mathbf{p},x^0) = \sqrt{F(\mathbf{p},x^0)\ddot{F}(\mathbf{p},x^0) - \dot{F}^2(\mathbf{p},x^0)} - \frac{1}{2}. \tag{2.22}$$

We will employ the distribution functions to define an effective dispersion relation

$$\omega(\mathbf{p},t) = \sqrt{\frac{\ddot{F}(\mathbf{p},t)}{-\det(g)F(\mathbf{p},t)}}, \tag{2.23}$$

which will be used to probe the structure of the excitations in the latter chapters.

2.1.3 Introducing Bjorken coordinates

Bjorken coordinates describe a longitudinally expanding geometry and are conceptionally similar to Rindler coordinates [55]. Here we would like to sketch a brief derivation and provide a motivation for the introduction of Bjorken coordinates. It is most convenient to start with a particle undergoing constant acceleration, whose tangent vector along its world line is

$$u^\mu = \begin{pmatrix} \gamma \\ \gamma v^i \end{pmatrix}.$$

Differentiation with respect to proper time τ defines the acceleration four vector a^μ:

$$\dot{u}^\mu = \frac{du^\mu}{d\tau} = \frac{dt}{d\tau}\frac{d}{dt}u^\mu = \gamma \begin{pmatrix} \dot{\gamma} \\ \dot{\gamma} v^i + \gamma a^i \end{pmatrix}.$$

Now we observe two facts: First, $u^\mu a_\mu = 0$ and second, $a^\mu a_\mu = \alpha^2$. The last statement is a direct consequence of requiring the acceleration to be constant while the first one follows from differentiating $u^\mu u_\mu = 1$. With both equations at our disposal, we strive to obtain expressions for α and $\dot{\gamma}$:

$$\dot{\gamma} = \gamma^3 a^i v_i, \tag{2.24a}$$
$$\alpha = a\gamma^3. \tag{2.24b}$$

To solve the last differential equation (2.24b), we need to integrate twice. If one chooses $v(t=0) = 0$ as an initial condition, one arrives at the velocity function

$$v(t) = \frac{\alpha t}{\sqrt{1+\alpha^2 t^2}}.$$

Integrating for a second time and considering $z(t=0) = \beta$, an explicit representation of the worldline can be found:

$$z(t) = \frac{1}{\alpha}\left(\sqrt{1+\alpha^2 t^2} - 1\right) + \beta. \tag{2.25}$$

Figure 2.2 shows a set of worldlines for different values of β and fixed acceleration α.

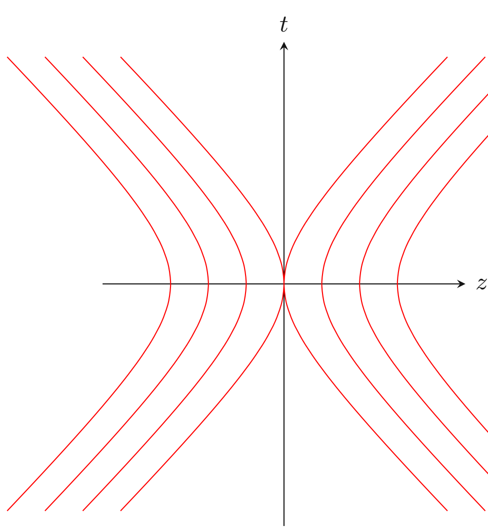

Figure 2.2: Hyperbolic worldlines as described by equation (2.25) of the constantly accelerated particle.

As we see, the worldlines of a constantly accelerated particle are hyperbolas. Next, we

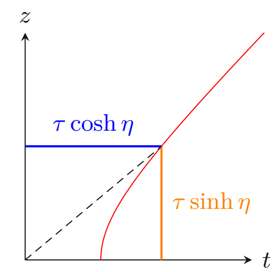

Figure 2.3: Schematic drawing to clarify the geometric origins of Bjorken coordinates. The variable η corresponds to the hyperbolic angle which is usually thought of as »rapidity«, while τ is the hyperbolic »radius« (from $z^2 - t^2 = \tau^2$) and identical to the proper time.

perform a change of coordinates from the static coordinates to the particle's proper time τ and (spatial) rapidity η. This leads in combination with figure 2.3 to the following definition of Bjorken coordinates:

$$\left.\begin{aligned} t &= \tau \cosh \eta \\ x &= x \\ y &= y \\ z &= \tau \sinh \eta \end{aligned}\right\} \Rightarrow ds^2 = d\tau^2 - \tau^2 d\eta^2 - dx^2 - dy^2.$$

To obtain the differential equation for the mode function in analogy to (2.8), we need to Fourier transform equation (2.3). Substituting the definition of the Bjorken coordinates, we arrive at

$$\left(\partial_\tau^2 + \frac{1}{\tau}\partial_\tau + p_T^2 + \frac{\nu^2}{\tau^2}\right) \xi_{p_T,\nu}(\tau) = 0. \tag{2.26}$$

The transverse momentum p_T and rapidity ν result from the Fourier modes $e^{\mathrm{i}p_T x_T}$ and $e^{\mathrm{i}\nu\eta}$ respectively.

2.2 Simulation details

We employ a well-probed numerical technique, namely classical–statistical lattice simulations. It is – as in our case – used to determine the structure of nonequilibrium dynamics of quantum field theories in their classicality limit. The validity of the classicality condition is achieved when the number of (bosonic) field quanta occupying a single mode is sufficiently large so that quantum fluctuations of the system can be neglected.

While the technique is equally suited to study gauge fields and scalar theories, we will restrict the mathematical description to the latter ones. This is appropriate since only scalar field theories are considered in the below chapters.

In order to set up the simulation, we needed to discretize the fields φ_a and their canonically conjugate momentum fields π_b on a three-dimensional lattice. These fields are then updated according to the Hamiltonian equations of motion (2.4).

We start our disquisition by considering the generating function (2.15). We will assign an individual field $\varphi^{\pm}$ to its respective time path $\mathcal{C}^{\pm}$ along the Schwinger-Keldysh-contour as described by figure 2.1, and introduce their action accordingly as

$$S_{\mathcal{C}}[\varphi] = S[\varphi^{+}] - S[\varphi^{-}].$$

Next, the mean field and the field difference are introduced as new variables. This will help us to distinguish between classical and quantum vertices later on. The following transformation is linear in the field variables:

$$\varphi = \frac{\varphi^{+} + \varphi^{-}}{2}, \qquad \tilde{\varphi} = \varphi^{+} - \varphi^{-} \qquad \Leftrightarrow \qquad \varphi^{+} = \frac{1}{2}\left(2\varphi + \tilde{\varphi}\right), \qquad \varphi^{-} = \frac{1}{2}\left(2\varphi - \tilde{\varphi}\right). \tag{2.27}$$

Hence, its Jacobi determinant is constant (in our case it is equal to one). The new action consists of the following three terms:

$$S_0[\varphi, \tilde{\varphi}] = \int d^4x \partial_\mu \tilde{\varphi}_a(x) \partial_\nu \varphi_a(x), \tag{2.28a}$$

$$S_{\text{int,cl}}[\varphi, \tilde{\varphi}] = -\frac{\lambda}{6N} \int d^4x \tilde{\varphi}_a(x) \varphi_a(x) \varphi_b(x) \varphi_b(x), \tag{2.28b}$$

$$S_{\text{int,qu}}[\varphi, \tilde{\varphi}] = -\frac{\lambda}{24N} \int d^4x \tilde{\varphi}_a(x) \tilde{\varphi}_a(x) \tilde{\varphi}_b(x) \varphi_b(x). \tag{2.28c}$$

The integral expression in equation (2.28a) might be transformed by the introduction of the total derivative:

$$\partial_\mu \left(\tilde{\varphi}_a \partial^\mu \varphi_a\right) = \partial_\mu \tilde{\varphi}_a \partial^\mu \varphi_a + \tilde{\varphi}_a \partial^2 \varphi_a.$$

Thus it becomes possible to use Gauß theorem (the ideas for the calculation is partly inspired by [56]) to further simplify (2.28a). Figure 2.4 provides insight into the following calculation(s): We imagine Minkowski space being decomposed into three-dimensional spacelike surfaces $\Sigma(t)$, whose normal vectors have to be timelike. Since n_ν is orthogonal to all vectors $\mathbf{v} \in \Sigma(t)$, forming the inner product with n_μ and an arbitrary vector w^μ extracts its time component

w^{0}[3]. Finally, the calculations go as follows:

$$\begin{aligned}
S_0[\varphi,\tilde{\varphi}] &= \int d^4x \left(\partial_\mu \left(\tilde{\varphi}_a \partial^\mu \varphi_a\right) - \tilde{\varphi}_a \partial^2 \varphi_a\right) \\
&= \int_{\Sigma(t_0)} d^3x\, \tilde{\varphi}_a \partial^\mu \varphi_a n_\mu - \int d^4x\, \tilde{\varphi}_a \partial^2 \varphi_a \\
&= \int_{\Sigma(t_0)} d^3x \tilde{\varphi}_a(t_0,\mathbf{x}) \partial_0 \varphi_a(t_0,\mathbf{x}) - \int d^4x \tilde{\varphi}_a \partial^2 \varphi_a.
\end{aligned}$$

The final term from above allows us to construct the classical action $S_{\mathrm{cl}}[\varphi,\tilde{\varphi}]$:

$$\begin{aligned}
S_{\mathrm{cl}}[\varphi,\tilde{\varphi}] &= \int d^4x\, \tilde{\varphi}_a \left(-\partial^2\varphi - \frac{\lambda}{6N}\varphi_a\varphi_b\varphi_b\right) \\
&= \int d^4x \tilde{\varphi}_a \frac{\delta S[\varphi]}{\delta \varphi_a} \\
&= -\int d^3x \tilde{\varphi}_a \partial_0 \varphi + S_0[\varphi,\tilde{\varphi}] + S_{\mathrm{int,cl}}[\varphi,\tilde{\varphi}].
\end{aligned}$$

As one observes, the classical action does not contain the $\tilde{\varphi}^3$ interaction term. The associated vertices are the ones that are neglected in the classical statistical approximation.

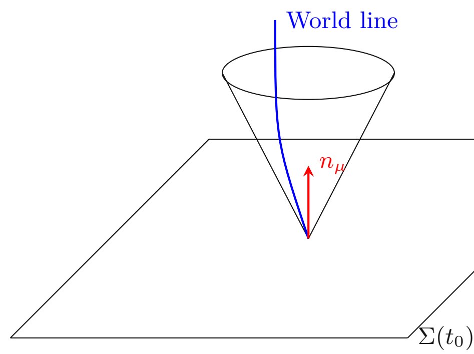

Figure 2.4: Constant time plane in four dimensional Minkowski space $\mathbb{M}_4$: The surface normal n_μ is timelike, i.e. $n_\mu n^\mu = 1$.

With the help of the Wigner distribution as described by [57], we are able to integrate

[3] $n_\mu w^\mu = n_0 w^0 - \underbrace{n_i w^i}_{=0} = n_0 w^0 \overset{n_0=1}{=} w^0$

over the initial density matrix:

$$\int [d\varphi^+][d\varphi^-]\langle\varphi^+|\rho_0|\varphi^-\rangle = \int [d\varphi_0][d\tilde{\varphi}_0]\langle\varphi_0 + \tilde{\varphi}_0/2|\rho_0|\varphi_0 - \tilde{\varphi}_0/2\rangle$$
$$= \int [d\varphi_0][d\tilde{\varphi}][d\pi_0]W[\varphi_0, \pi_0]e^{\mathrm{i}\int d^3x\pi_0\tilde{\varphi}_0}.$$

With the help of the field variable transformation and the above result, the generating functional of equation (2.15) becomes

$$Z[J, R; \rho_0] = \int [d\varphi_0][d\pi_0]W[\varphi_0, \pi_0] \int \mathcal{D}'\varphi\mathcal{D}\tilde{\varphi} \exp\left(\mathrm{i}\int_{t_0} d^4x\tilde{\varphi}_a \frac{\delta S}{\delta\varphi_a} + S_{\mathrm{int,qu}}[\varphi, \tilde{\varphi}] + \mathrm{sources}\right), \tag{2.29}$$

where the sources involve a series of linear and bilinear terms with regards to J_a and R_{ab}. Neglecting the quantum vertex allows us to analytically integrate the generating function. Hence, we write down the classical partition function as

$$Z^{\mathrm{cl}} = \int [d\varphi_0][d\pi_0]W[\varphi_0, \pi_0]\Big|_{\varphi=\varphi^{\mathrm{cl}}}. \tag{2.30}$$

Now we can calculate the average over an observable $O[\varphi, \pi]$ in analogy to classical statistical mechanics:

$$\int [d\varphi_0][d\pi_0]W[\varphi_0, \pi_0]O[\varphi^{\mathrm{cl}}(\varphi_0, \pi_0), \pi^{\mathrm{cl}}(\varphi_0, \pi_0)]. \tag{2.31}$$

In a nutshell, the core part of the simulation revolves around solving the classical equations of motions for the Bjorken-expanding background

$$(\partial_\tau^2 - \partial_T^2 - \frac{1}{\tau^2}\partial_\nu^2 + \frac{1}{\tau}\partial_\tau)\varphi_b + \frac{\lambda}{3!N}(\varphi_a\varphi_a)\varphi_b = 0, \tag{2.32}$$

where $\partial_T^2 = \partial_x^2 + \partial_y^2$ and calculating various correlation functions as statistical averages from the fields.

Linearized fluctuations

We follow the approach laid out by [58, 59]: In order to compute the spectral function, we need to exploit the relationship between the retarded two-point correlator and ρ.

$$G_R(t, t', p_T, \nu) = \theta(t - t')\rho(t, t', p_T, \nu). \tag{2.33}$$

We can extract G_R by linearizing equation (2.32), i.e. we will split the field φ_b into the background field φ_b^{BG} and the linear fluctuation field $\delta\varphi_b$. This leads to the linearized equation of motion:

$$(\partial_\tau^2 - \partial_T^2 - \frac{1}{\tau^2}\partial_\nu^2 + \frac{1}{\tau}\partial_\tau)\delta\varphi_b + \frac{\lambda}{3!N}(\varphi_a^{\mathrm{BG}}\varphi_a^{\mathrm{BG}} + 2\varphi_a^{\mathrm{BG}}\varphi_b^{\mathrm{BG}})\delta\varphi_b = 0. \tag{2.34}$$

Next, we need to perturb (2.34) with a source term $j_a(x)$ that acts as an inhomogeneity to the linearized equation. The expectation value of the fluctuation field is the convolution of the retarded Green's function — the two-point correlator — with the source term:

$$\langle\delta\varphi_b(x)\rangle = \int d^4\tilde{x}\, G_{R,bc}(x,\tilde{x})j_c(\tilde{x}). \tag{2.35}$$

In a spatially homogenous system, we can perform a coordinate transformation to $(\mathbf{x}+\tilde{\mathbf{x}})/2$ and $\Delta\mathbf{x} = \mathbf{x}-\tilde{\mathbf{x}}$ and neglect the former coordinate due to spatial homogeneity and approximate boost invariance. Fourier transformation of (2.35) with respect to the spatial coordinates leads to

$$\langle\delta\varphi_b(t,\mathbf{p})\rangle = \int d\tilde{t}\, G_{R,bc}(t,\tilde{t},\mathbf{p})j_c(\tilde{t},\mathbf{p}). \tag{2.36}$$

in Fourier space. If we choose the source $j_c = j_c^0\delta(\tilde{t}-t_{\mathrm{pert}})$, the expectation value of the fluctuation field is described by:

$$\langle\delta\varphi_b(t,\mathbf{p})\rangle = G_{R,bc}(t,t_{\mathrm{pert}})j_c^0(t,\mathbf{p}). \tag{2.37}$$

Finally, we need to fix the source j_c^0 such that the canonical commutation relations are fulfilled. To this end, we demand for random Gaussian source fields:

$$\langle j_a^0(\mathbf{p})(j_b^0(\mathbf{q}))^*\rangle_j = V\delta_{\mathbf{p},\mathbf{q}}\delta_{ab}. \tag{2.38}$$

Hence, we arrive at the retarded part of the spectral function ρ:

$$\theta(t-\tilde{t})\rho(t,\tilde{t},p) = \frac{1}{VN}\left\langle\langle\delta\varphi_b(t,\mathbf{p})\rangle_{\mathrm{cl}}(j_b^0(\mathbf{q}))^*\right\rangle_j. \tag{2.39}$$

The time-derivative of the spectral function is defined as

$$\theta(t-\tilde{t})\dot{\rho}(t,\tilde{t},p) = \frac{1}{VN}\left\langle\langle\delta\pi_b(t,\mathbf{p})\rangle_{\mathrm{cl}}(j_b^0(\mathbf{q}))^*\right\rangle_j. \tag{2.40}$$

Chapter 3

Summary of previous results in a nonexpanding geometry

While there exists a rich literature regarding nonequilibrium dynamics in a non–expanding background, the extraction of the statistical correlator and spectral function of a scalar theory in a Bjorken-expanding geometry was not yet tried. In this chapter, we will give a brief overview of already known results in Minkowski spacetime and compare them to our own reproductions.

We will start with an analysis of the different scaling regions and proceed to the nonequal-time correlators. The properties of the scaling regions are determined by the single-particle distribution function $f(p,t)$, or — more accurately speaking — by the exponents α and β of the rescaled distribution function $t^{\alpha} f_S(t^{\beta} p)$.

To probe the physics, we employ classical statistical lattice simulation as described in section 2.2 to study systems with one temporal and three spatial dimensions.

3.1 Universality classes far from equilibrium

The evolution of a quantum system depends to a certain degree on its initial conditions. Choosing them to be close to thermal equilibrium, the system relaxes until it reaches thermal equilibrium. But with far-from-equilibrium initial conditions — these are usually realized in situations where occupation numbers are large, i.e. $f \gg 1$ so the system becomes highly correlated — the time evolution becomes more complex. Before the quantum system reaches thermal equilibrium, it might approach a nonthermal fixed point. Such points are usually characterized by looking at a quantity $C(x; s)$ (usually C is obtained from the two-point correlators). If C exhibits a certain scaling behavior, namely

$$C(x; s) = s^{\alpha} h(x/s), \tag{3.1}$$

where h is the scaling function and α the respective scaling exponent, the system is called self-similar [60]. We detect such cases by analyzing the properties of the single-particle distribution function: In the proximity of a nonthermal fixed point, f shows a self-similar behavior so the distribution becomes time-independent and we can safely describe it with the scaling function f_S.

The critical exponents α and β together with the scaling and distribution function will be the focus of this section before we move to the nonequal-time excitations.

In figure 3.1, we show the typical behavior of the distribution function f in a double-logarithmic plot. We can approximate $f(p,t)$ with the scaling function

$$f_S(p) \sim p^{-\kappa},$$

where we detected that the value of κ should be $3/2$ in the intermediate momentum region. We quote from the literature (vid. [61]): The numerical values for the critical exponents α and β are:

$$\alpha = -4/5 \qquad \text{and} \qquad \beta = -1/5.$$

Hence, we have uniquely determined our universality class for the intermediate momentum region using the distribution function $f(p,t)$.

3.2 Unequal time excitations

In this section, we will examine the statistical and spectral functions in the intermediate momentum regime described in section 3.1. We will compare the results with data from the literature.

We performed ten simulations of an $O(4)$-symmetric scalar field theory with the same initial parameters and averaged over the Fourier-transformed curves. The background field is initialized according to a Gaussian distribution ($f(p,t_0) = n_0 e^{-p^2/2}$) whose initial amplitude was $n_0 = 35$. Furthermore, a 192^3-point lattice was used with a spacing of $a = 0.5$. The simulation starts at $t_0 = 0$ and lasts for $t \leq 2000$. A single linear fluctuation is used to perturb the simulation at $t_{\text{pert}} = 1000$ and the time evolution of the response field is studied as a function of $\Delta t = t - t_{\text{pert}}$.

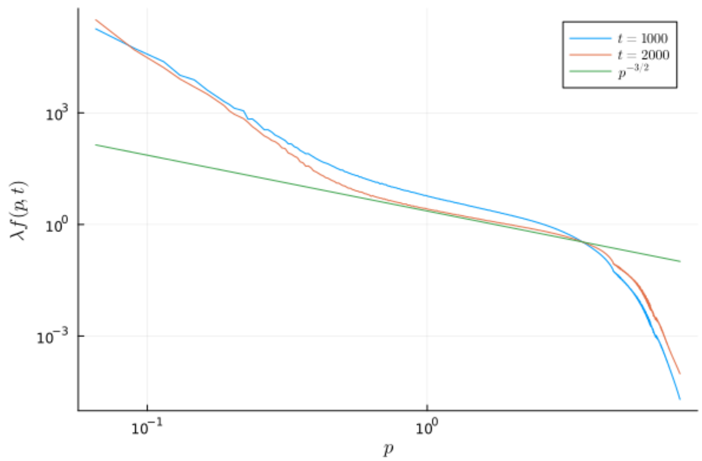

Figure 3.1: Double-logarithmic plot of the single-particle distribution function calculated according to (2.22) at different times $t = 1000$ and $t = 2000$. The intermediate momentum regime follows a power law with $f(p,t) \sim p^{-3/2}$.

Considering the time-domain signal in figure 3.2, we choose the upper boundary of the Fourier transformation[1] to be $\Delta t_{\max} = 300$. The signal exhibits strong damping, which in effect leads to the structure of the curves in frequency space shown in Fig. 3.3: They have a large, single quasiparticle peak, which is symmetric around the maximum. This is a well-established fact from the literature (vid. [59]): $O(N)$ scalar field theories tend to have a dominant Lorentzian peak if $N \geq 3$.

The spectral function and the statistical correlator satisfy a generalized fluctuation-dissipation relation. The Kubo-Martin-Schwinger condition for bosons is given by

$$F(p^0, \mathbf{p}, t) = -\mathrm{i} \left(n_B(p^0) + \frac{1}{2} \right) \rho(p^0, \mathbf{p}, t), \tag{3.2}$$

where n_B is the well-known Bose-Einstein distribution function. In our situation, it becomes possible to drop the 1/2 and expand n_B into a series. At the lowest order, this leads to

$$n_B(\omega) = \frac{1}{e^{\beta\omega} - 1} \approx \frac{1}{\beta\omega} \approx \frac{T}{\omega}.$$

Plugging the result from above into equation (3.2), we arrive at a relation between the

[1]For more details of the numerical Fourier transform, see appendix A

temperature T and the nonequal-time correlators in frequency space:

$$F(\omega) = -\mathrm{i}\frac{T}{\omega}\rho(\omega).$$

Considering the well-known formulæ for the Fourier transformation of the derivatives, we arrive at

$$\ddot{F}(\omega) = \dot{\rho}(\omega)T.$$

That is, we expect our correlators to approximately lie on top of each other, where we have to note that the statistical correlator F has to be rescaled by the factor $F^{-1}(\Delta t = 0)$.

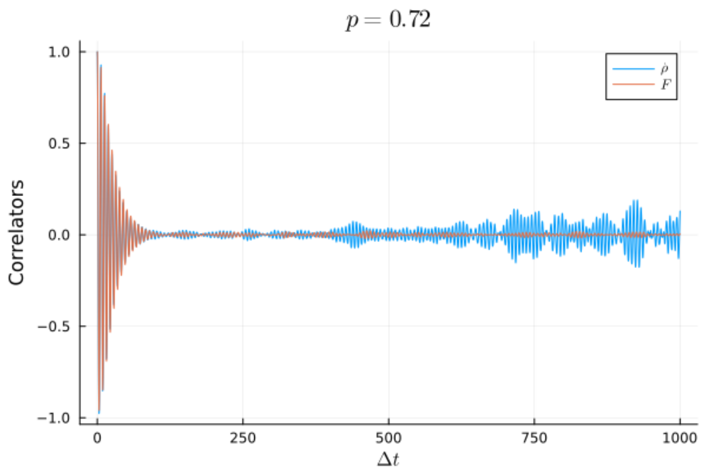

Figure 3.2: Signals from the unequal time correlators in the time domain: We detect that while the statistical correlator F falls off to zero quite fast, the spectral function becomes noisy.

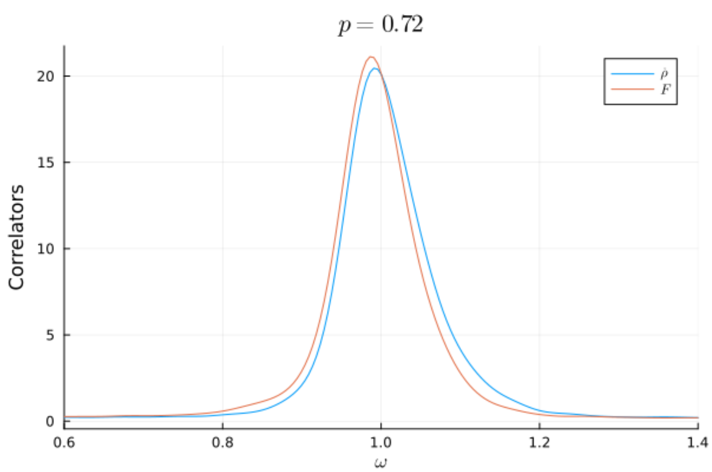

Figure 3.3: Spectral function $\dot\rho$ and statistical correlator F of a nonexpanding scalar theory: The correlators satisfy the generalized fluctuation-dissipation relation.

Chapter 4

Free theory

Before we consider interaction, we will focus our attention on the details concerning the free relativistic (massless) scalar field theory. As will be shown in this chapter, the free field theory in a Bjorken-expanding geometry provides interesting insights into the physics of the excitation spectrum and allows us to judge the validity of the numerical simulation.

To this end, we will take a closer look at equation (2.26): Its solutions — calculated for different transversal momenta p_T and rapidity wave number ν — are compared to the late–time expansion of the mode function introduced in this chapter. The analytical computations are finally contrasted with the numerical results obtained from a classical statistical lattice simulation.

The main conclusions drawn from this disquisition are:

1. The rescaled spectral function $\dot{\rho}$ and statistical correlator F satisfy the fluctuation–dissipation–relation.

2. The effects of the background geometry lead to a redshift with regard to the oscillation frequency of the excitations.

4.1 Unequal time correlation function

The statistical correlator is calculated as proscribed by equation (2.17), while the computation of the spectral function involves a more complex mathematical framework since the commutator of two classical fields reduces to the Poisson brackets. Hence linear response theory — as described in [58], [62], [59]— is used to obtain ρ. In figure 4.1, the bare statistical and spectral functions are compared to the rescaled versions obtained according to

$$\dot{\rho} \to \frac{\dot{\rho}}{\sqrt{2\omega\tau}}, \tag{4.1}$$

$$F \to \sqrt{2\omega\tau}F. \tag{4.2}$$

To explain the rescaling, we need to dive into the details of the numerical simulation. We considered the following correlators corresponding to the respective definition of the statistical correlator and spectral function and their respective time-derivatives:

$$\dot{\rho}(\tau', \tau) \sim \langle \delta\pi(\tau')\delta\pi(\tau) \rangle,$$
$$F(\tau', \tau) \sim \langle \Phi(\tau')\Phi(\tau) \rangle.$$

By inspection of the definitions 2.10, we can perform the calculation of the unequal time correlator from above. It leads to

$$F \propto \xi(\tau')\xi(\tau) = \frac{1}{\sqrt{2\omega(\tau')\tau'}} \frac{1}{\sqrt{2\omega(\tau)\tau}} e^{\mathrm{i}(\Omega(\tau')-\Omega(\tau))},$$

where we introduced the late-time expression for the mode function [23],

$$\xi_{\mathrm{late}}(\tau) = \frac{1}{\sqrt{2\omega\tau}} e^{\mathrm{i}\Omega(\tau)} = \frac{1}{\sqrt{2\omega\tau}} \exp\left(\mathrm{i}\int_{\tau_0}^{\tau} \omega(p_T, \nu, t)\, dt\right), \tag{4.3}$$

with ω as the dispersion relation in the Bjorken background

$$\omega(p_T, \nu, \tau) = \sqrt{m^2(\tau) + p_T^2 + \frac{\nu^2}{\tau^2}}.$$

Since we are only varying proper time τ, while holding the perturbation time τ' fixed, all terms containing only τ' are constants that can be discarded[1]. To analyze only the oscillatory term, it is necessary to multiply by $\sqrt{2\omega(\tau)\tau}$.

In the case of the spectral function, we need to perform the proper time derivative. From (4.3), we conclude that

$$\dot{\xi} = \mathrm{i}\omega\xi.$$

Using definition 2.10 again, we establish the above rescaling of the spectral function.

[1]We are allowed to discard all constant terms because all correlators were normalized so that they start at 1.

Next, we will vindicate our rescaling by looking at the time signals from the simulation. We chose rather small lattices with 96 points in the transversal direction and 256 in the longitudinal one. As usual, an $O(4)$ theory is considered with initial mass $m = 0$. The simulation starts at $\tau_0 = 1000$ and is perturbated immediately after. As expected, the rescaled statistical correlator and the time derivative of the spectral function are identical, since (2.34) effectively simplifies the classical equation of motion. The result is proved in figure 4.1, where both correlators from a general mode are compared to their respective rescaled versions.

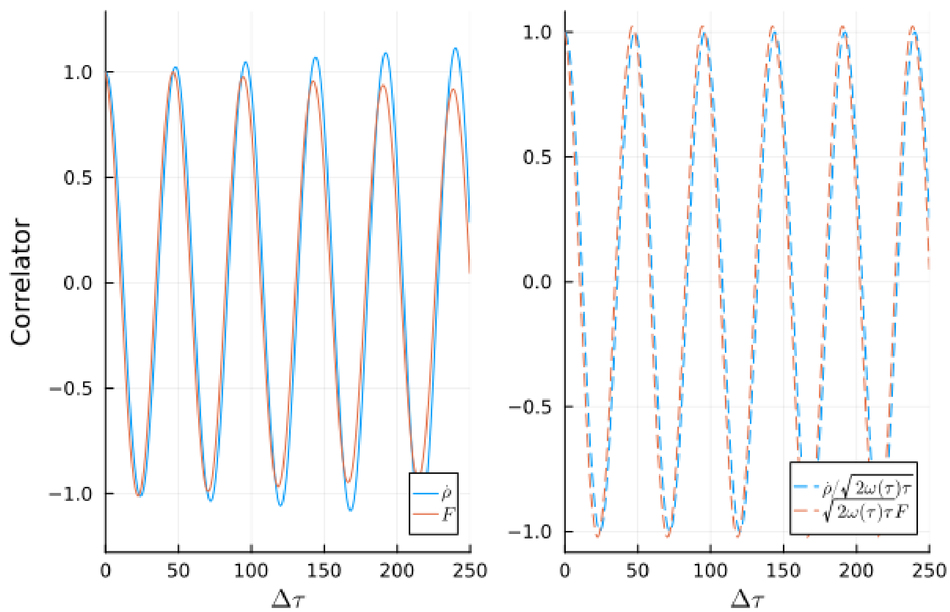

Figure 4.1: Comparison of the »bare« spectral function and statistical correlator of a transverse mode (left picture) with the rescaled versions (right): The rescaled functions are essentially identical to one another, that is, they satisfy the fluctuation-dissipation-relation. Note that F has been normalized to one by dividing it by $F(\Delta\tau = 0)$.

4.2 Spectral functions in the free theory

Next, we set the initial amplitude to zero and compared the results with the analytical calculations. As a side note: Since $n_0 = 0$, the background field is and remains zero for the entire simulation. Hence, we cannot extract the statistical correlator due to the fact that it is calculated from the background fields, but the spectral function is obtained from the linearized fields, whose initial amplitudes are nonzero. Since there is no damping in the free field theory, it is strictly speaking not possible to calculate the fast Fourier transformation of the correlator.

We begin our disquisition by considering equation (2.26) that will lead to three different cases with regard to the dynamical behavior of the modes. The mode function $\xi_{p_T,\nu}(\tau)$ depends on the transversal momentum and the rapidity. By setting one of them to zero, we achieve a different dynamical behavior which provides us some insight into the physics of a scalar theory in an expanding background.

4.2.1 Transverse mode

We call all modes with $p_T \neq 0$ and $\nu = 0$ transverse. Their dynamic is governed by

$$\left(\partial_\tau^2 + \frac{1}{\tau}\partial_\tau + p_T^2\right)\xi_{p_T} = 0.$$

The perturbation kicks in at late times ($\tau_{\mathrm{pert}} = 1000$), hence we can safely neglect the $\frac{1}{\tau}$ term[2]. Thus the differential equation will be identical to the non-expanding case and the solutions are simple plain waves — considering the symmetry of the correlators, the odd sine components have to vanish — $\xi_{p_T} \sim \cos(p_T \Delta\tau)$[3], which is in accordance with the late-time expansion if the initial mass m is assumed to be zero[4]. The result is validated by figure 4.2.

4.2.2 Longitudinal mode

Setting $p_T = 0$ and $\nu \neq 0$ results in longitudinal modes. We make the ansatz $\xi_\nu = \tau^\alpha$ and arrive at the solution

$$\xi_\nu(\tau) = C\tau^{\mathrm{i}\nu} + D\tau^{-\mathrm{i}\nu}.$$

By setting $C = 0$ and $D = 1/\tau_0^{-\mathrm{i}\nu}$, we arrive at the same result as by computation of the integral in (4.3). Dropping all odd components of the mode function, we obtain

$$\xi_\nu(\tau) \sim \cos\left(\nu \ln(\tau/\tau_0)\right).$$

Due to the logarithmic increase of proper time in the cosine wave, a visible redshift is observed in figure 4.3. This effect results from the nonzero rapidity as a consequence of the expansion in the longitudinal direction.

[2] The most general solutions are in fact Bessel functions.

[3] For clarity: »$\sim$« means »without nonoscillating prefactors like $\sqrt{2\omega(\tau)\tau}$.«

[4] This approximation is in our case valid since we set the initial mass $m_0 = 0$ at the beginning of our simulation.

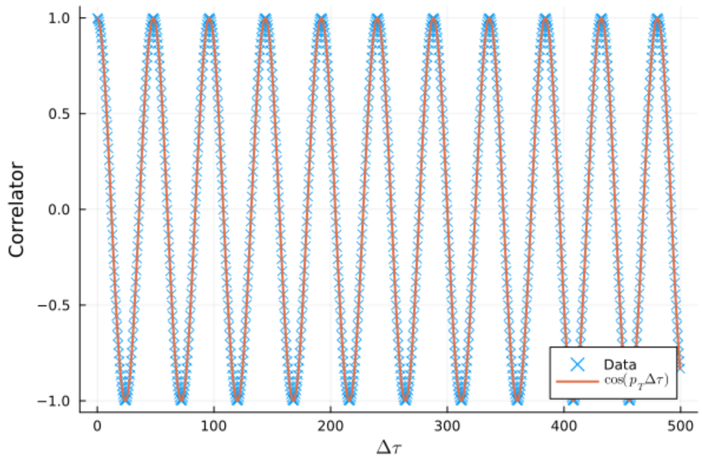

Figure 4.2: Transverse mode: The rescaled correlator ($\dot{\rho}$) is a plain cosine function. This is in accordance with our expectation: The transverse modes in the free theory should behave in the same way as in the nonexpanding case.

4.2.3 General mode

Setting neither p_T nor ν to zero results in a general mode: They require us to solve equation (2.26) in full generality: The solution to it is the Hankel function of the second kind $H^{(2)}_{\mathrm{i}\nu}(p_T\tau)$. In this case, the late-time approximation differs from the analytical solution of the linearized equation of motion. This is only natural since the calculation of the Hankel function at an imaginary order is numerically quite involved.

Depending on the values of p_T and ν, we can observe a redshift effect that is usually weaker compared to the longitudinal modes. The same is true of the overall damping effect as shown in figure 4.4. The form of ξ_{late} captures the evolution of this mode quite well.

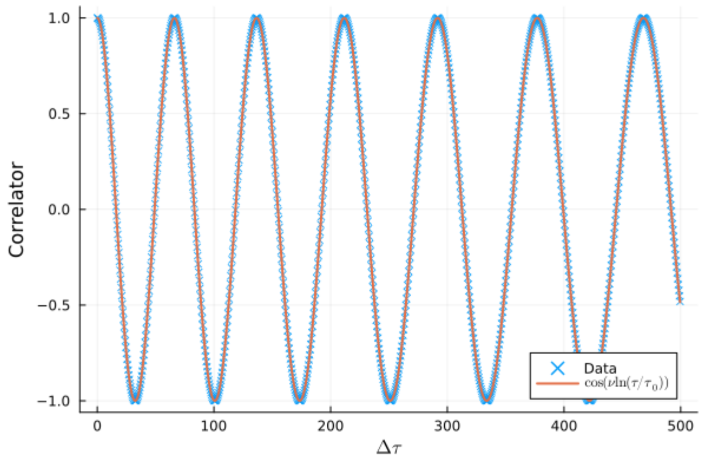

Figure 4.3: Longitudinal mode: The redshift due to the ν^2/τ^2 term in (2.34) is clearly visible.

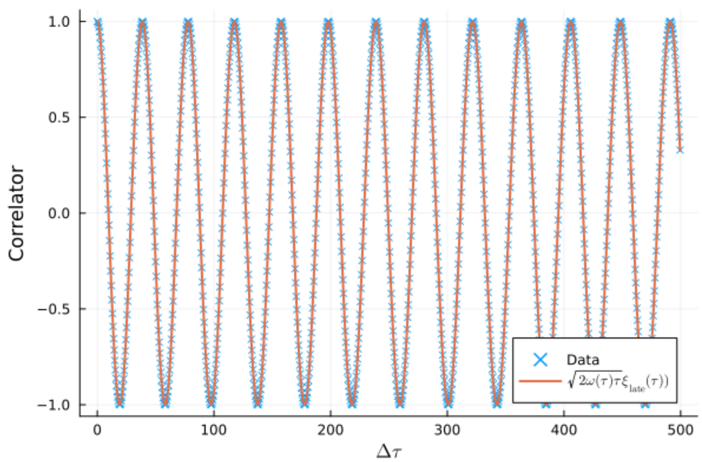

Figure 4.4: General mode: The redshift in the oscillation frequency is still present, although the effect is weaker compared to the longitudinal modes.

4.3 Summary

In this chapter, we studied the free scalar theory and compared different set of modes. We have found that transverse modes behave in the same way as one expects them to behave in a nonexpanding background geometry. The effects of the background geometry are only relevant for the longitudinal and the general modes. The mode function in the transverse case behaves as if the background geometry were flat. As shown in figures 4.3 and 4.4, Bjorken expansion results in a redshift of the frequency and causes a damping effect.

It is possible to remove the effects of the damping by rescaling the correlators as shown in (4.2). We will use the rescaled spectral and statistical functions in the next chapter in order to obtain smooth Fourier-transformed excitations.

Chapter 5

The interacting theory

In the previous chapter, we discussed the free field theory by setting the coupling parameter λ to zero. In the following part of this thesis, we consider an interacting massless scalar theory with an $O(4)$ symmetry. We chose the φ^4–potential as our interaction term.

To this end, we start with an investigation of equal time correlators, i.e. the particle distribution function and the dispersion relations before analyzing the statistical correlator and spectral function for different modes. We chose the energy range between the infrared and the ultraviolet regime. The universality class of this region bears a structural similarity compared to the same momentum regime in gauge theories [3].

The main part of this chapter (Sec. 5.3) revolves around the computation and analysis of the excitations: Depending on the momentum modes, we obtain statistical and spectral functions with different properties that we fitted with Lorentz functions in order to discern the quasiparticle structure of the excitations.

5.1 Distribution function and critical exponents

Dynamic scaling properties are usually described by the time-dependent distribution function $f(p_T, \nu, \tau)$ obtained from equation (2.22). In the longitudinally expanding geometry, the single-particle distribution depends on the transversal momentum p_T, rapidity ν and proper time τ. The scaling regime is determined from the critical exponents α, β and γ introduced via the time–independent scaling functions f_S. The parameter α is used to describe the scaling of proper time τ, while transversal and longitudinal momentum are rescaled by β and γ:

$$f(p_T, \nu, \tau) = \tau^{\alpha} f_S(\tau^{\beta} p_T, \tau^{\gamma} p_z). \tag{5.1}$$

The scaling behavior is influenced by the expansion, i.e. particle number density decreases as the system expands with a rate proportional to $1/\tau$. This means particle number conservation is expressed by $\tau n \sim$ const. The same conservation law holds true for the energy density of the system.

The following graphics are obtained by employing a classical statistical lattice simulation with overoccupied initial conditions, with an initial amplitude $n_0 = 35$ for the Gaussian distribution $f(p, t_0) = n_0 e^{-p^2/2}$ and initial proper time $\tau_0 = 1000$. The $96^2 \times 2056$ lattices had a longitudinal spacing of $a_\nu = 2.5 \cdot 10^{-4}$ and a transversal one of $a_T = 0.5$. All dimensional quantities are made dimensionless by multiplying them with suitable powers of Q.

In figure 5.1, we show the single-particle distribution at three different times. Three different regions were observed and their properties were studied in [23]. In order to examine the different power laws corresponding to the different momentum regions, $f(p_T, \nu, \tau)$ is plotted over a double logarithmic scale. It is clearly visible that the distribution function follows a $p_T^{-\kappa}$-law, where $\kappa = 1$, in the intermediate momentum regime. This contrasts with the results found in section 3.1, where κ was determined to be $3/2$.

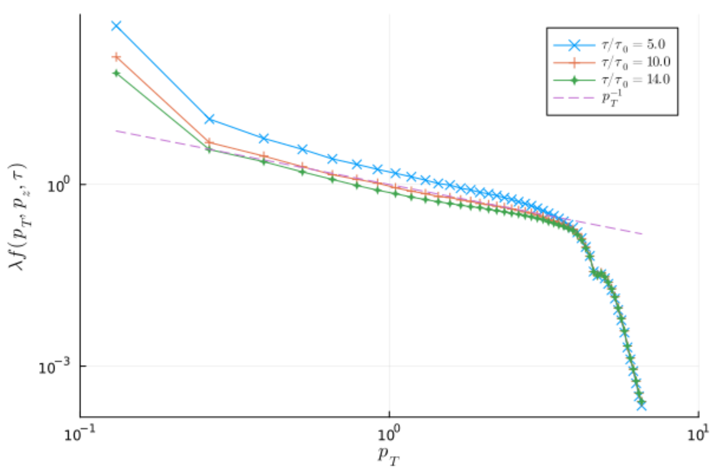

Figure 5.1: Time-dependent single-particle distribution plotted logarithmically for different times. The dashed line shows that the intermediate momentum regime follows an inverse–power–law. The rapidity, at which f is evaluated, is zero.

With the help of equation (5.1), we find by matching the critical exponents α and β a self–similar evolution in the intermediate momentum regime of the single-particle distribution function. Our results for α and β are given by

$$\alpha = 0.67 \qquad \text{and} \qquad \beta = 0.0.$$

The rescaled distribution is shown in figure 5.2.

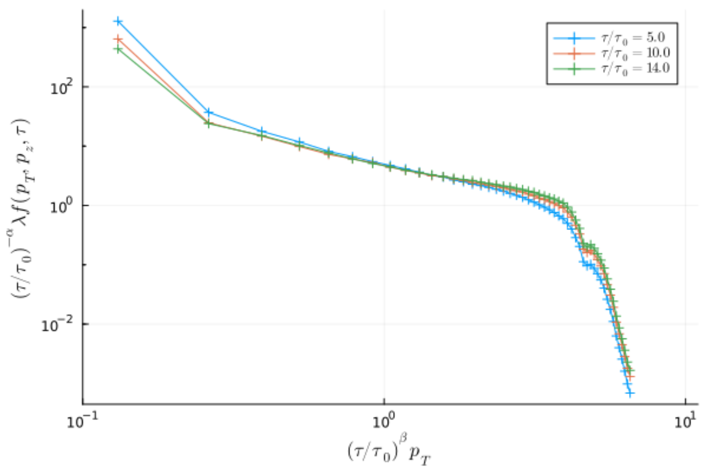

Figure 5.2: Log-log plot of the rescaled distribution function plotted over transversal momentum at a fixed longitudinal momentum.

The same procedure is again employed to extract the third critical exponent γ. We take note of the fact that $f(p_T = const, \nu, \tau)$ does not follow a power-law behavior as seen in Fig. 5.3. The underlying cause is the redshift that is due to the expansion in the longitudinal direction and the momentum broadening due to the interactions. The best result with regard to the exponent matching is obtained by choosing $\gamma = 0.38$. The rescaled distribution is shown in figure 5.4.

We conclude that the scaling exponents match the results from the literature (vid. [61]), which are given by

$$\alpha = -2/3, \qquad \beta = 0, \qquad \gamma = 1/3.$$

The same exponents and power-law behavior classify the intermediate momentum regime (in fact, it is not only the intermediate momentum regime but basically all of it down to the mass scale) in an expanding gauge theory.

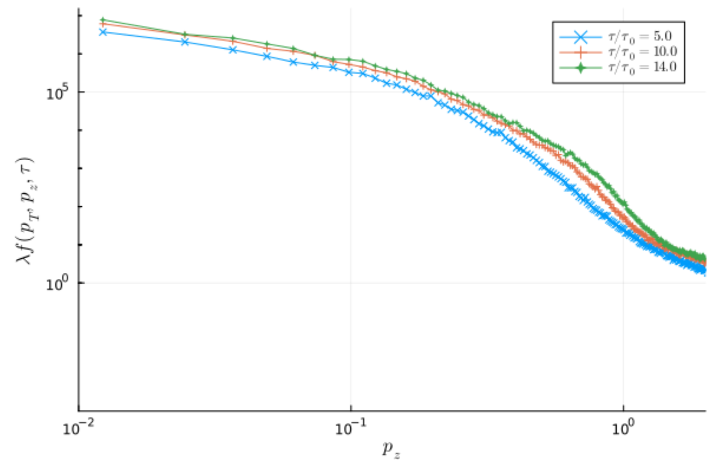

Figure 5.3: Distribution function plotted over the longitudinal momentum. The single-particle distribution function does not follow a power-law in this case.

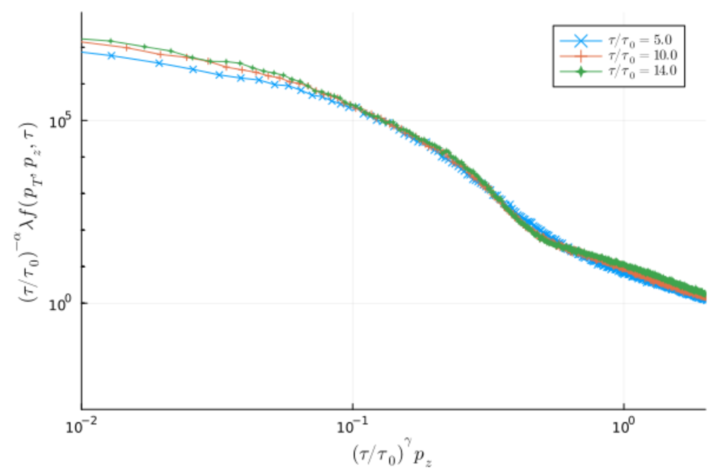

Figure 5.4: Rescaled distribution corresponding to figure 5.3.

5.2 Dispersion

From equation (2.23), we obtained a series of dispersion relations at different times τ that are well approximated by

$$\omega(\mathbf{p}, \tau) = \sqrt{p_T^2 + \frac{\nu^2}{\tau^2} + m^2(\tau)}. \tag{5.2}$$

Since the above equation is in essence the relativistic energy-momentum-relation, we might think of the resulting excitations as relativistic quasiparticles. This is an interesting result for it suggests that ω is essentially independent of the angle $\theta = \arctan(p_T/p_z)$ and hence solely described by the absolute value of the momentum vector (p_T, p_z). Such a behavior is usually only expected in an isotropic background.

Figure 5.5 shows the dispersion relation extracted from the simulation in comparison to the dispersion form in (5.2) fitted to the data. It is clearly visible that the dynamically generated mass $m(\tau)$ shrinks as time progresses. From the literature ([61]) we know that the evolution of the thermal mass follows

$$m(\tau) \sim \tau^{-\frac{1}{3}}.$$

This behavior is a result of particle number conservation which holds even in an expanding background.

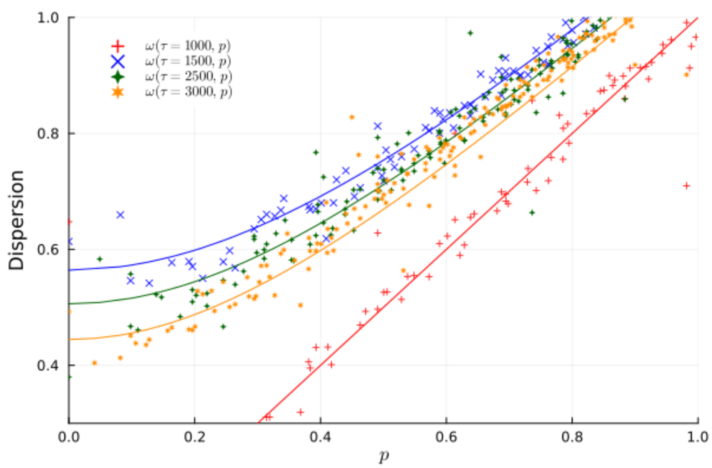

Figure 5.5: Dispersions relations at different times τ. The simulation starts at $\tau = 1000$, hence a linear relation results due to the thermal mass $m(\tau)$ being zero. Lines with the same color as the data points correspond to their respective fit.

5.3 Nonequal-time excitations

In this section, we shift our focus onto the essential nonequal–time correlators. We will primarily analyze the spectral function since it encodes the nature of the peaks, their energy and their lifespan. A large obstacle to understanding our numerical data lies in the nature of the Fourier transformation in a longitudinally expanding background. This is by and large related to the redshift effect described in section 4.2 contrasting with the usage of plane waves as kernel of the Fourier transformation. By perturbing the simulation early on and choosing a small time window of the data to transform, we were able to extract the physical properties of different sets of spectral functions and statistical correlators. We mainly focused on the following characteristics of the excitation structure:

The full width at half maximum (FWHM) can be extracted from the structure of the excitations in frequency space. We always calculate the FWHM of the main peak in the excitation spectrum of the spectral functions, since it is directly related to the lifetime of the observed quasiparticle structure:

$$\gamma = \mathrm{FWHM} \propto \frac{1}{\tau_{\mathrm{life}}}.$$

We think of the FWHM as the damping rate γ that allows us to determine if a quasiparticle lives long enough to »feel« an interaction before decaying.

To examine the overall properties of the peaks, we performed data fitting with a linear combination of Lorentzian curves defined via

$$f_{\mathrm{fit}}(\omega) = \sum_i \frac{A_i}{\pi} \frac{\gamma_i/2}{(\omega - \omega_{0_i})^2 + (\gamma_i/2)^2}. \tag{5.3}$$

We chose the fit function in a way so that the damping parameters γ_i correspond to the FWHMs of their respective peaks.

5.3.1 Transverse modes

The structure of the excitations in case of transverse modes ($p_T \neq 0$, $\nu = 0$) should be — at least according to their dynamics governed by 2.34 — similar to the ones found in the Minkowski case. Indeed, with regard to the modes we probed, we detected one large quasiparticle peak in frequency space as seen in figure 5.7. This is in accordance with the time-domain data shown in figure 5.6, which exhibits an exponential damping before collapsing to zero.

Note that the time signals of the correlators were rescaled according to the prescriptions laid down by equations (4.1) and (4.2). The Fourier-transformed curves were obtained from the rescaled functions.

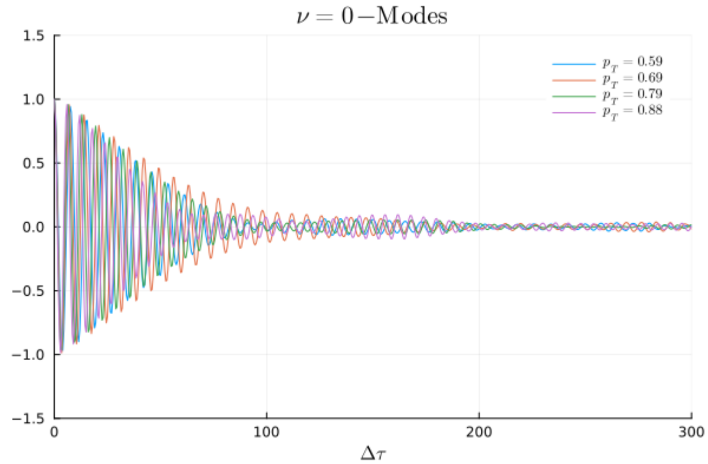

Figure 5.6: Spectral functions ($\dot{\rho}$) for different values of p_T in the time domain. We show the part of the signal that we use for the Fourier transformation.

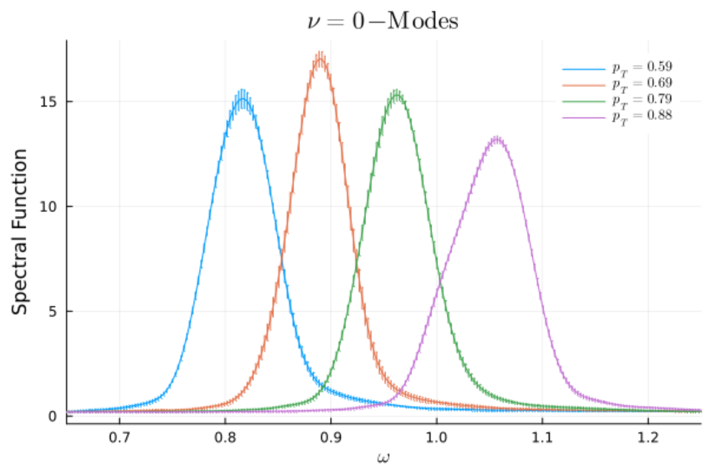

Figure 5.7: Fourier-transformed results of the data in Fig. 5.6: The transverse modes show a large Lorentzian peak in frequency space.

We examined to effect of the time window $\Delta\tau_{\text{window}}$ used to Fourier transform our data. In this way, we could detect if the truncation of the time signal does not change the physical structure of the correlators in frequency space. Figure 5.8 shows the spectral function of two different transverse momentum modes calculated at five different time windows. The curves lie nearly on top of each other if $\Delta\tau \geq 300$, which is in perfect accordance with the shape of the time domain data from figure 5.6.

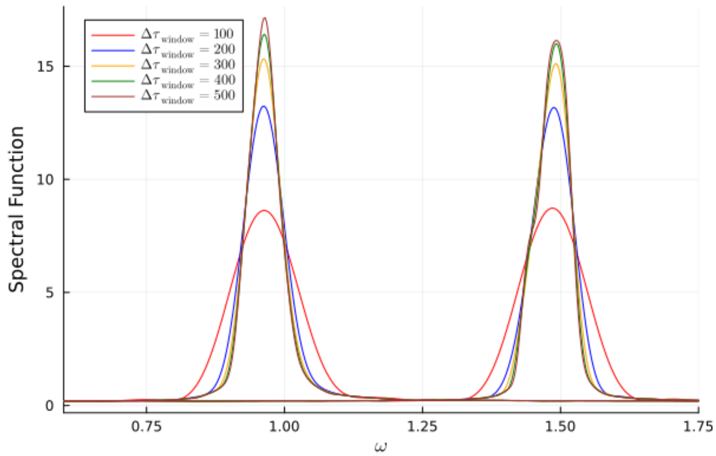

Figure 5.8: $\dot{\rho}$ for different time windows. The left curve corresponds to a $p_T = 0.78$-mode, while the right one was calculated at $p_T = 1.37$. The results indicate that a truncation at $\Delta\tau_{\text{window}} \approx 300$ does not change the outcome drastically.

Interestingly, if we take a closer look at the damping rates γ (i.e. the FWHM) extracted from these curves, we can clearly see that they follow the same pattern, regardless of the size of $\Delta\tau_{\text{window}}$, although we note that the patterns become more pronounced if the time window is increased, as it can be observed in figure 5.9.

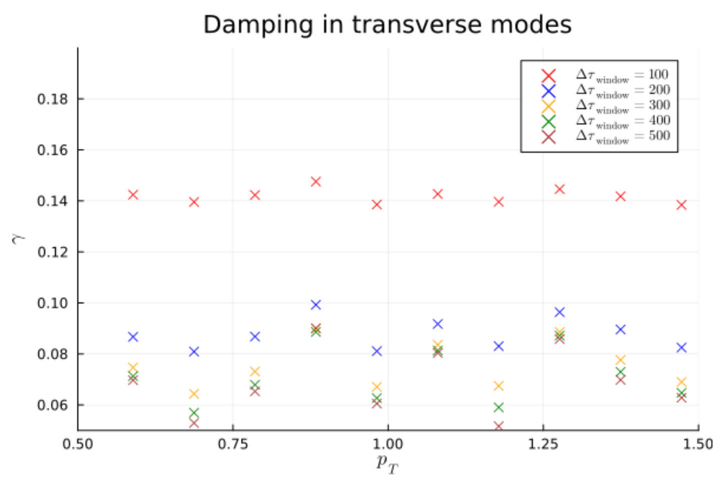

Figure 5.9: The damping rates taken at different time windows follow the same pattern. We note that the pattern itself is difficult to describe since no clear behavior emanates from it.

Lastly, we fitted different transverse modes with a single Lorentz curve as described by eq. (5.3). Figure 5.10 only partially vindicates our assumption that the quasiparticle structure is Lorentzian in nature: The Lorentz curve does not fit the tails of the excitation peak well, which might be due to the truncation of the time signal or because of a different curve structure.

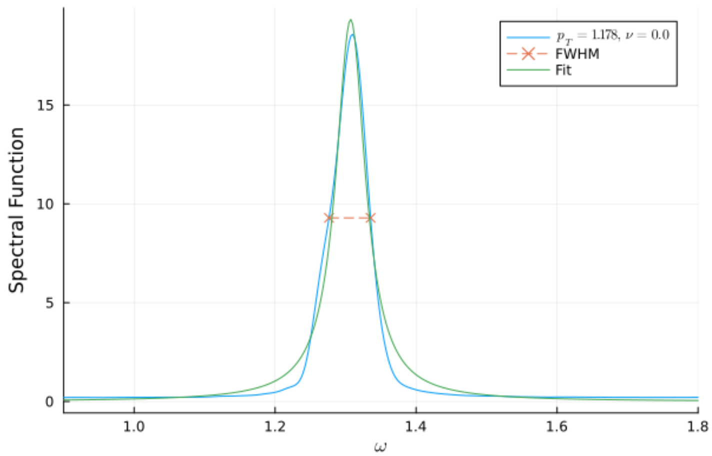

Figure 5.10: Fiting with a single Lorentz curve: The Lorentz curve captures the symmetry properties quite well, but it does not fit with the tails of the peak. The calculated damping rate from the fit is $\gamma \approx 0.051$, which is in accordance with our results from figure 5.9.

5.3.2 Longitudinal modes

The time signal from the longitudinal modes ($\nu \neq 0$, $p_T = 0$) is shown in figure 5.11. The $p_z = 0.16$-mode behaves somewhat distinctively: Its damping is comparatively slow and does not show an exponential pattern. The cause of this behavior is the comparatively small value of p_z. We expect from the rest of the modes that they show a single quasiparticle peak, which is vindicated by figure 5.12. All probed longitudinal excitations are asymmetric around the maximum. The lifetime of the quasiparticles increases with increasing momentum, which is observed from the broadening of the peaks.

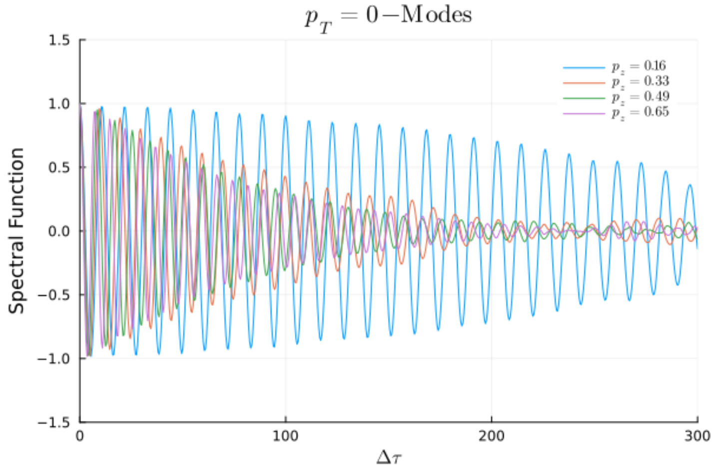

Figure 5.11: Spectral function from longitudinal modes in the time-domain: Due to the small value of p_z, the blue curve exhibits weaker damping compared to the other modes.

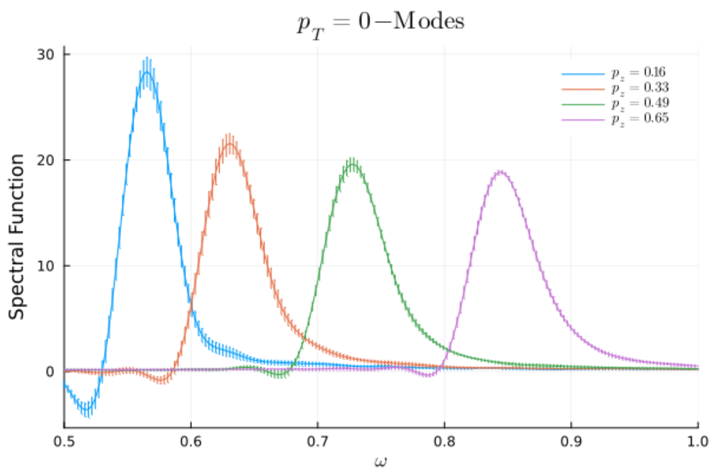

Figure 5.12: Fourier-transformed curves of figure 5.11. The blue curve (and to some degree, the orange one too) has a small negative peak.

In order to examine the negative peak from the blue curve in Fig. 5.12, we performed data fitting using two Lorentzian curves as described by equation (5.3). The result is shown in figure 5.13: We note that the smaller negative peak might occur due to the redshift of the frequency. This explains, why the modes associated with larger p_z values, do not tend to exhibit a negative peak.

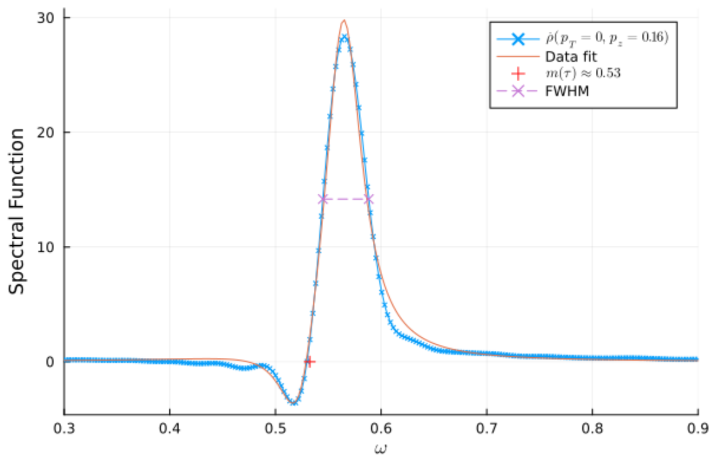

Figure 5.13: Spectral function of a longitudinal mode: We can clearly see that the small negative excitation happens around the red plus sign, i.e. where $\omega \approx m(\tau)$. The FWHM calculated from the original data is 0.0434, which compares quite well with the γ-parameter ($\gamma \approx 0.0428$) associated with the main peak.

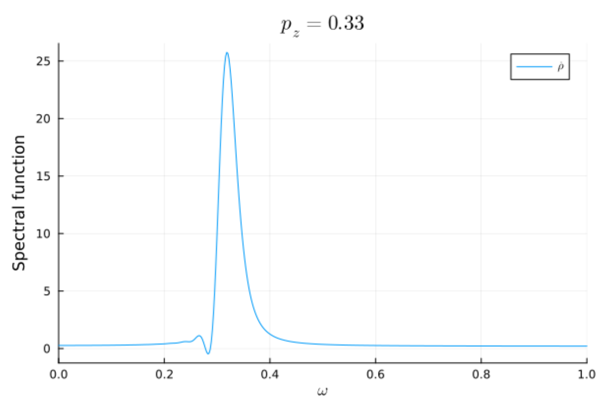

Figure 5.14: Fourier transform of (5.4): The small negative peak is likely the result of a frequency redshift due to the longitudinal expansion.

From the results in section 4.2.2, we compared the longitudinal modes with the Fourier transformation of a damped oscillation

$$e^{-|\Delta\tau|\gamma} \cos\left(\nu \ln\left(\frac{\tau_0 + |\Delta\tau|}{\tau_0}\right)\right). \tag{5.4}$$

The results are shown in figures 5.12 and 5.14. They are highly indicative that the negative peak observed in the longitudinal modes has its origin in the logarithmic increase of proper time as described by equation (5.4). This phenomenon is visible even in the free theory and is therefore an effect of the background geometry.

Applying the same strategy as in the previous subsection, we find that we are allowed to truncate the time domain data at approximately $\Delta\tau \approx 400$. Figure 5.15 shows the evolution of the Fourier-transformed spectral function when the time window is changed. We take note that although the structure of the longitudinal excitations is different compared to the transverse modes, and insofar as these differences arise due to the effects of the Bjorken-expansion, we can still apply the same techniques (i.e. the plane wave Fourier transform) to extract spectra from the simulation data.

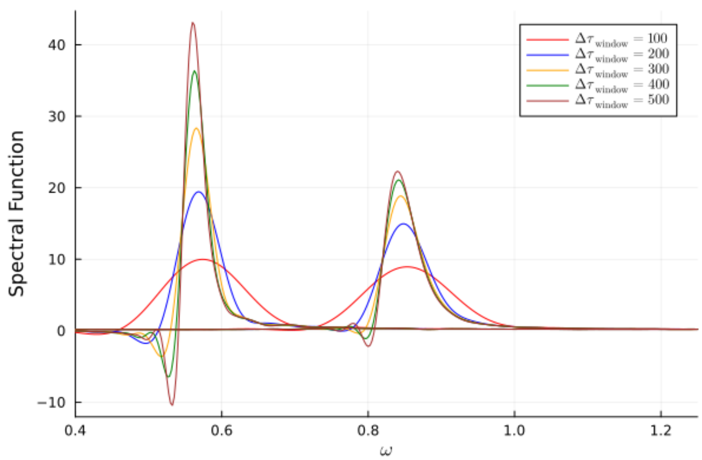

Figure 5.15: $\dot{\rho}$ of longitudinal modes calculated at different time windows. Here we detect that it is advisable to use a slightly larger time window for the smaller wave numbers (the left curve was taken at $\nu = 245.4$ or $\nu/\tau = 0.16$) while at higher wave numbers ($\nu = 981.75$ or $\nu_\tau = 0.65$, right graph) smaller $\Delta\tau_{\text{window}}$ might be employed.

The damping rates follow the same pattern irrespective of the values of $\Delta\tau_{\text{window}}$ that was used to calculate the frequency space signals. But unlike in the case of the transverse excitations, we can clearly observe that the damping rates slowly increase with longitudinal momentum, that is, we expect the quasiparticles related to the longitudinal excitations to decay faster if the wave number ν becomes larger.

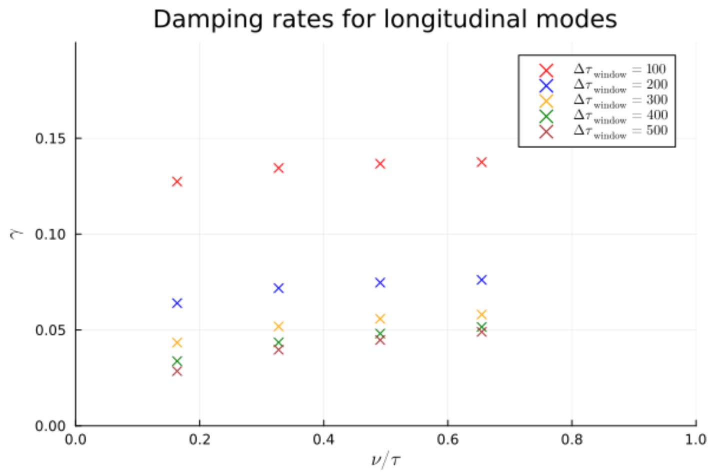

Figure 5.16: In case of longitudinal modes, the damping γ monotonically increases with the longitudinal momentum.

5.3.3 General modes

Modes, where both p_T and ν are nonzero, tend to behave more like longitudinal modes if ν dominates or like transverse modes if $p_T > p_z$. This is in accordance with our observations from section 4.2.3. Hence we will discuss results that are valid for all probed excitations. Before we dive into the details, we take note that the statistical correlator is rescaled according to the scheme laid down by equations (4.2) and (4.1). F needs to be divided by $F(\Delta\tau = 0)$ in order to normalize it to one. The similarity of the statistical correlator and the spectral function is vindicated by figure 5.17, i.e. all modes abide by the generalized Kubo-Martin-Schwinger condition to good accuracy.

We use the maxima of the large Lorentzian peaks of the spectral and statistical functions to reconstruct the dispersion relation. Figure 5.18 shows that the maxima accurately match their position on the dispersion curve as defined by the equal time correlators from (2.23).

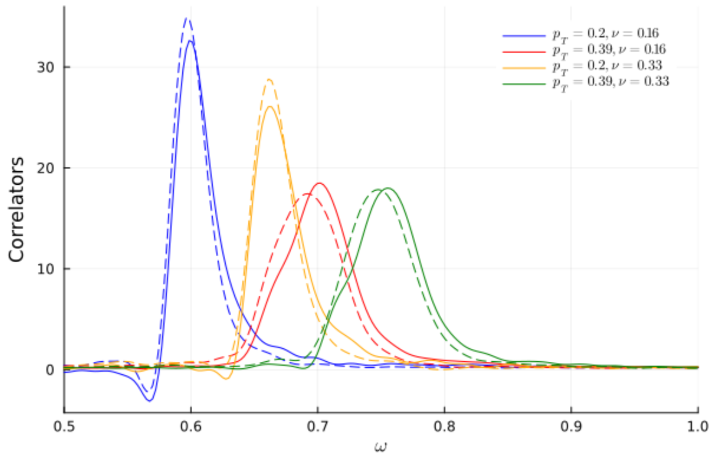

Figure 5.17: Comparison of different modes: The dashed lines represent the statistical correlator F, the continuous ones the spectral function $\dot{\rho}$. From this result, we conclude that the normalized correlators satisfy the generalized fluctuation-dissipation-relation.

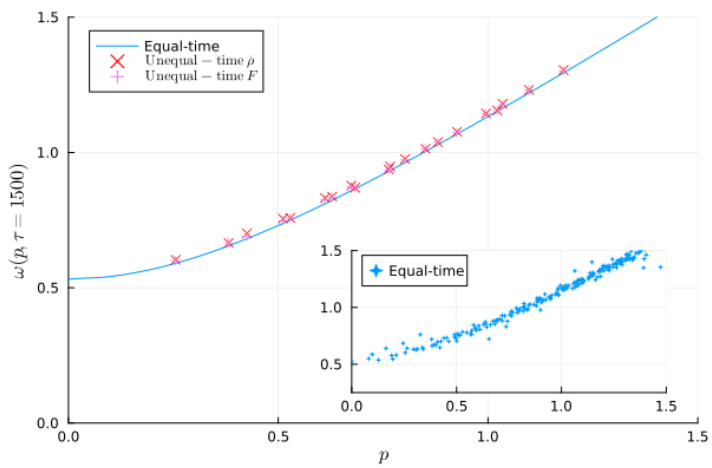

Figure 5.18: Dispersion relation obtained from the maxima of $\dot{\rho}$ and F compared to the »equal-time dispersion« at time $\tau = 1500$.

5.4 Summary

In this chapter, we studied the intermediate momentum universality class and its excitations of the interacting theory using classical statistical lattice simulations. As shown in figures 5.2

and 5.4, the $O(4)$ exhibits universal scaling behavior in the intermediate momentum regime. Within the limits of this universality class, we extracted the nonequal-time correlators for different sets of modes using the following categorization:

- $p_T \neq 0$ and $\nu = 0$ — Transverse Modes,
- $p_T = 0$ and $\nu \neq 0$ — Longitudinal Modes,
- $p_T \neq 0$ and $\nu \neq 0$ — General Modes.

We analyzed the peak structure and the damping of the above modes and detected a remarkable difference in the excitation spectrum of transverse and longitudinal modes, while the general modes tend to lie between the former edge cases. The transverse modes showed large single excitation peaks that are symmetric around the maximum. The damping rates γ do not follow a consistent pattern, as seen in figure 5.9. In contrast, longitudinal modes show an asymmetric peak that might be approximated by a linear combination of two Lorentz curves. At lower momenta, the curves exhibit a small negative peak as shown in figure 5.12. The damping rate slightly increases with the momenta, but it is generally smaller compared to the transverse excitations. We argued that the difference occurs due to the redshift effect of the longitudinal expansion that is visible even in the free theory.

Surprisingly, the calculation of the spectral and statistical function failed in cases where the perturbation time τ_{pert} was significantly larger than the initial time τ_0. We collected the results of late-time simulations in appendix B, although it remains unclear why the excitations exhibit such an unphysical spectrum. One of the causes might be the difficulty of developing an analog to the Fourier transformation in a Bjorken-expanding spacetime since due to the redshift of the frequency, the plane wave expansion is strictly speaking not well defined. A too large time window might pose a further problem since the metric of the Bjorken geometry changes with proper time τ.

Chapter 6

Conclusion

The core of this thesis revolves around the analysis of the excitation spectrum of relativistic scalar field theories in a longitudinally expanding geometry. While classical statistical simulations on the real-time lattice were employed to study the properties of gauge theories (vid. [58], [63]), scalar theories lived in the shadows of the former. Nevertheless, a rich set of literature exists about the dynamics of bosonic many-body systems with overoccupied initial conditions (e.g. [10]). The numerical technique itself is well-probed judging from previous works.

In this chapter, we will summarize the results of the simulations and try to give an outlook on possible future developments with regard to scalar and gauge theories.

Before we probed the interacting theory, we analyzed signals in the time domain obtained from the free theory. We detected that the transverse modes behave in a similar way compared to the ones obtained in a Minkowski background. Due to the $(\nu/\tau)^2$-term, the longitudinal modes behave differently: They show a distinct redshift, which is in accordance with our analytic analysis. Finally, we examined a general mode, where we detected a similar behavior as for the longitudinal modes, but the former exhibited a weaker redshift and a higher oscillation frequency, depending on the ratio of p_T and ν/τ.

With regards to the interacting theory, we started our disquisition by examining the equal time correlators, focusing our attention on the single-particle distribution function $f(p_T, \nu, \tau)$. We derived different universality classes from it by examining its rescaled analogon and its associated scaling exponents. After comparing our results with the established literature, we chose the intermediate momentum regime, since it falls into the same universality class as gauge fields. Then the unequal-time correlators were examined: We detected a qualitative difference between longitudinal and transverse modes. While the transverse modes behave very similar to those in a nonexpanding system, the longitudinal modes are asymmetric around the maximum of the main peaks. A small negative excitation emerging for longitudinal modes is also observed, which is the result of the redshift due to the logarithmic increase of proper time τ.

We want to point out that the excitation spectrum at late times appears to be highly pathological, as shown in appendix B. The underlying cause of this problematic behavior remains unclear and needs further examination. It has to be noted that all our results are obtained from the classical dynamics of the scalar field theory, which lack genuine quantum effects, hence limitting the applicability of classical-statistical methods.

Finally, we need to reconsider that the focus of this work lies in the study of relativistic scalar fields. Further research focusing on the unequal-time correlators in an expanding geometry of gauge theories is needed in order to compare the excitation spectrum of the intermediate momentum universality class of the two microscopically different theories.

Appendix A

Fast Fourier Transform

The study of quasiparticle excitations encourages us to transform the signal from the time domain to the frequency domain. To this end, we employ fast Fourier transformations (FFTs). To mirror the conditions of our simulations, we need to perform a linear transformation with regard to the time arguments t and t_{pert}: By introducing the meantime $\bar{t} = (t + t_{\text{pert}})/2$ and the time difference $\Delta t = t - t_{\text{pert}}$, we arrive at the following equations for the (analytical) transformation:

$$F(\bar{t}, \omega, p) = 2 \int_0^\infty d\Delta t \cos(\omega \Delta t) F(\bar{t} + \Delta t/2, \bar{t} - \Delta t/2, p),$$
$$\rho(\bar{t}, \omega, p) = 2 \int_0^\infty d\Delta t \sin(\omega \Delta t) \rho(\bar{t} + \Delta t/2, \bar{t} - \Delta t/2, p).$$

Since significant difficulties would be introduced by performing an analytic transformation, we need to approximate it numerically. This is done by choosing concrete upper integration boundary $\Delta t_{\max}$. Finally, we approximate $\bar{t}$ with t, which is allowed if t is sufficiently large. The numerical transformation reads now as

$$F(\bar{t}, \omega, p) \approx 2 \int_0^{\Delta t_{\max}} d\Delta t \cos(\omega \Delta t) F(\bar{t} + \Delta t, \bar{t}, p),$$
$$\rho(\bar{t}, \omega, p) \approx 2 \int_0^{\Delta t_{\max}} d\Delta t \sin(\omega \Delta t) \rho(\bar{t} + \Delta t, \bar{t}, p).$$

The implementation details are outlined in [64].

To smoothen the result of the Fourier transformation, we applied zero padding and a Hann windowing function defined in equation (A.1).

$$w(t) = \frac{1 + \cos(2\pi t)}{2} \tag{A.1}$$

A typical time signal of a general mode accompanied by its Fourier transform is shown in figure A.1.

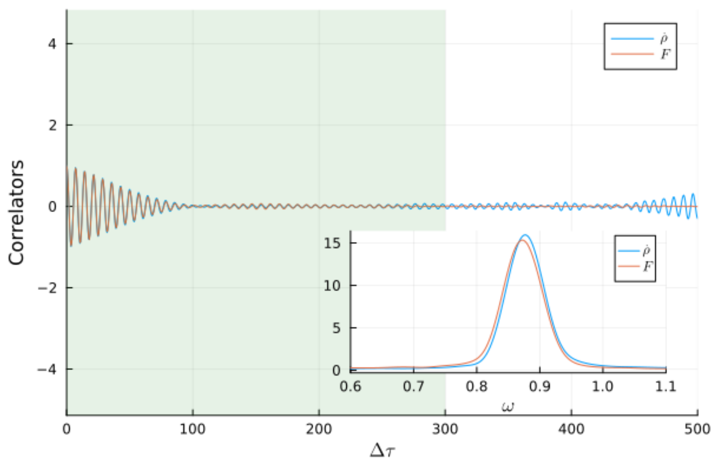

Figure A.1: Choosing the integration limit in the time domain: The statistical correlator sharply falls off to zero while the spectral function tends to diverge. The transformation is applied to the data between 0 and $\Delta\tau_{\max} = 300$, yielding two smooth curves in frequency space.

Appendix B

Pathological excitations

At late times, it was impossible to reconstruct physically sound correlation functions from the simulation. While it remains unclear whether numerical artifacts or the nature of the plane wave Fourier transform are the cause for these results, we are nevertheless going to show the spectral function and the statistical correlator. From equation (2.34) we could establish three different dynamical situations by adjusting transversal momentum p_T and rapidity ν. But strikingly, in all tested cases, the correlators show the same pathological structures, even if $\nu = 0$. In the last case, we would expect approximately similar results compared to the flat Minkowski background, since the damping term ν^2/τ^2 vanishes. This, at least, points in the direction of some underlying numerical issues with the expanding lattice.

The simulation was performed on lattice consisting of $96^2 \times 2048$ points, with a transverse spacing parameter $a_T = 0.5$ and longitudinal spacing $a_L = 2.5 \cdot 10^{-4}$. We started our numerical experiment at $\tau_0 = 1000$, while the perturbation happened at $\tau_{\text{pert}} = 10000$, lasting till $\tau_{\max} = 14000$, and averaged over 40 simulations, lest the result is distorted by statistical errors.

The resultant signals — both in the time and frequency domain — are shown in figure B.1, from which the reader may observe that the correlator functions exhibit a complex oscillatory pattern that slowly approaches zero as time increases. Compared to the excitation in figure A.1, we take notice of a complex oscillation pattern leading to a severely jagged signal in frequency space. The Fourier-transformed signal in Fig. B.2 is taken from a general node. We note that all modes, regardless of their p_T and ν values, show the kind of excitation structure as described in the referenced figure.

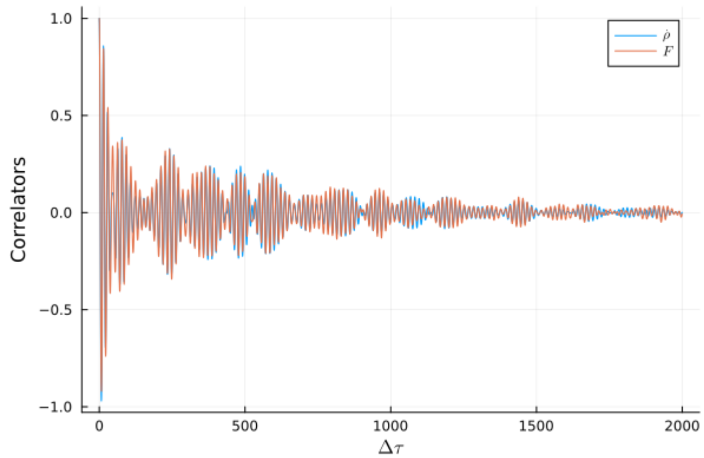

Figure B.1: Pathological spectral function and statistical correlator obtained from a »late-time« ($t_{\text{pert}} = 10000$) simulation.

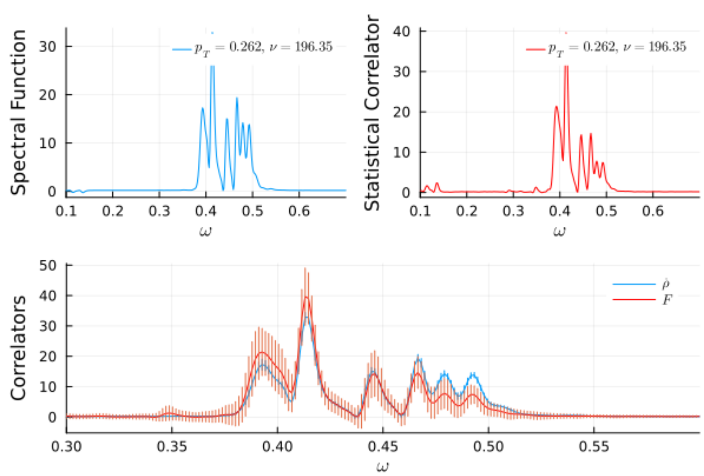

Figure B.2: Fourier-transformed data from B.1: Although the correlators show unrealistic excitations they appear to be satisfying the fluctuation-dissipation-relation.

Bibliography

[1] P. C. Hohenberg and B. I. Halperin. "Theory of dynamic critical phenomena". In: *Rev. Mod. Phys.* 49 (3 July 1977), pp. 435–479. DOI: 10.1103/RevModPhys.49.435. URL: https://link.aps.org/doi/10.1103/RevModPhys.49.435.

[2] Christian-Marcel Schmied, Aleksandr N. Mikheev, and Thomas Gasenzer. "Non-thermal fixed points: Universal dynamics far from equilibrium". In: *International Journal of Modern Physics A* 34.29 (Oct. 2019), p. 1941006. ISSN: 1793-656X. DOI: 10.1142/s0217751x19410069. URL: http://dx.doi.org/10.1142/S0217751X19410069.

[3] J. Berges et al. "Universality Far from Equilibrium: From Superfluid Bose Gases to Heavy-Ion Collisions". In: *Physical Review Letters* 114.6 (Feb. 2015). ISSN: 1079-7114. DOI: 10.1103/physrevlett.114.061601. URL: http://dx.doi.org/10.1103/PhysRevLett.114.061601.

[4] J. Berges et al. "Turbulent thermalization process in heavy-ion collisions at ultrarelativistic energies". In: *Physical Review D* 89.7 (Apr. 2014). ISSN: 1550-2368. DOI: 10.1103/physrevd.89.074011. URL: http://dx.doi.org/10.1103/PhysRevD.89.074011.

[5] J. Berges et al. "Universal attractor in a highly occupied non-Abelian plasma". In: *Physical Review D* 89.11 (June 2014). ISSN: 1550-2368. DOI: 10.1103/physrevd.89.114007. URL: http://dx.doi.org/10.1103/PhysRevD.89.114007.

[6] Jürgen Berges, Alexander Rothkopf, and Jonas Schmidt. "Nonthermal Fixed Points: Effective Weak Coupling for Strongly Correlated Systems Far from Equilibrium". In: *Physical Review Letters* 101.4 (July 2008). ISSN: 1079-7114. DOI: 10.1103/physrevlett.101.041603. URL: http://dx.doi.org/10.1103/PhysRevLett.101.041603.

[7] Jürgen Berges and Gabriele Hoffmeister. "Nonthermal fixed points and the functional renormalization group". In: *Nuclear Physics B* 813.3 (June 2009), pp. 383–407. ISSN:

0550-3213. DOI: 10.1016/j.nuclphysb.2008.12.017. URL: http://dx.doi.org/10.1016/j.nuclphysb.2008.12.017.

[8] Raphael Micha and Igor I. Tkachev. "Turbulent thermalization". In: *Physical Review D* 70.4 (Aug. 2004). ISSN: 1550-2368. DOI: 10.1103/physrevd.70.043538. URL: http://dx.doi.org/10.1103/PhysRevD.70.043538.

[9] D. T. Son. "Reheating and thermalization in a simple scalar model". In: *Physical Review D* 54.6 (Sept. 1996), pp. 3745–3761. ISSN: 1089-4918. DOI: 10.1103/physrevd.54.3745. URL: http://dx.doi.org/10.1103/PhysRevD.54.3745.

[10] Boris Nowak, Dénes Sexty, and Thomas Gasenzer. "Superfluid turbulence: Nonthermal fixed point in an ultracold Bose gas". In: *Physical Review B* 84.2 (July 2011). ISSN: 1550-235X. DOI: 10.1103/physrevb.84.020506. URL: http://dx.doi.org/10.1103/PhysRevB.84.020506.

[11] Michal P. Heller, Aleksas Mazeliauskas, and Thimo Preis. "Prescaling Relaxation to Nonthermal Attractors". In: *Physical Review Letters* 132.7 (Feb. 2024). ISSN: 1079-7114. DOI: 10.1103/physrevlett.132.071602. URL: http://dx.doi.org/10.1103/PhysRevLett.132.071602.

[12] Sebastian Erne et al. "Universal dynamics in an isolated one-dimensional Bose gas far from equilibrium". In: *Nature* 563.7730 (Nov. 2018), pp. 225–229. ISSN: 1476-4687. DOI: 10.1038/s41586-018-0667-0. URL: http://dx.doi.org/10.1038/s41586-018-0667-0.

[13] Stefan Lannig et al. *Observation of two non-thermal fixed points for the same microscopic symmetry*. 2023. arXiv: 2306.16497 [cond-mat.quant-gas].

[14] Maximilian Prüfer et al. "Observation of universal dynamics in a spinor Bose gas far from equilibrium". In: *Nature* 563.7730 (Nov. 2018), pp. 217–220. ISSN: 1476-4687. DOI: 10.1038/s41586-018-0659-0. URL: http://dx.doi.org/10.1038/s41586-018-0659-0.

[15] E. Nicklas et al. "Observation of Scaling in the Dynamics of a Strongly Quenched Quantum Gas". In: *Physical Review Letters* 115.24 (Dec. 2015). ISSN: 1079-7114. DOI: 10.1103/physrevlett.115.245301. URL: http://dx.doi.org/10.1103/PhysRevLett.115.245301.

[16] Martin Gazo et al. *Universal Coarsening in a Homogeneous Two-Dimensional Bose Gas*. 2024. arXiv: 2312.09248 [cond-mat.quant-gas].

[17] Timon A. Hilker et al. "First and Second Sound in a Compressible 3D Bose Fluid". In: *Physical Review Letters* 128.22 (June 2022). ISSN: 1079-7114. DOI: 10.1103/physrevlett.128.223601. URL: http://dx.doi.org/10.1103/PhysRevLett.128.223601.

[18] Lena H. Dogra et al. "Universal equation of state for wave turbulence in a quantum gas". In: *Nature* 620.7974 (July 2023), pp. 521–524. ISSN: 1476-4687. DOI: 10.1038/s41586-023-06240-z. URL: http://dx.doi.org/10.1038/s41586-023-06240-z.

[19] Yuri V. Kovchegov and Eugene Levin. *Quantum Chromodynamics at High Energy*. Vol. 33. Oxford University Press, 2013. ISBN: 978-1-00-929144-6, 978-1-00-929141-5, 978-1-00-929142-2, 978-0-521-11257-4, 978-1-139-55768-9. DOI: 10.1017/9781009291446.

[20] T. Lappi. "Production of gluons in the classical field model for heavy ion collisions". In: *Phys. Rev. C* 67 (2003), p. 054903. DOI: 10.1103/PhysRevC.67.054903. arXiv: hep-ph/0303076.

[21] François Gelis, Tuomas Lappi, and Raju Venugopalan. "High energy scattering in Quantum Chromodynamics". In: *International Journal of Modern Physics E* 16.09 (Oct. 2007), pp. 2595–2637. ISSN: 1793-6608. DOI: 10.1142/s0218301307008331. URL: http://dx.doi.org/10.1142/S0218301307008331.

[22] Paul C. Martin and Julian Seymour Schwinger. "Theory of Many-Particle Systems. I". In: *Physical Review* 115 (1959), pp. 1342–1373. URL: https://api.semanticscholar.org/CorpusID:122306641.

[23] J. Berges et al. "Nonequilibrium fixed points in longitudinally expanding scalar theories: Infrared cascade, Bose condensation, and a challenge for kinetic theory". In: *Physical Review D* 92.9 (Nov. 2015). ISSN: 1550-2368. DOI: 10.1103/physrevd.92.096006. URL: http://dx.doi.org/10.1103/PhysRevD.92.096006.

[24] Gert Aarts and Jürgen Berges. "Classical Aspects of Quantum Fields Far from Equilibrium". In: *Physical Review Letters* 88.4 (Jan. 2002). ISSN: 1079-7114. DOI: 10.1103/physrevlett.88.041603. URL: http://dx.doi.org/10.1103/PhysRevLett.88.041603.

[25] Sangyong Jeon. "Boltzmann equation in classical and quantum field theory". In: *Physical Review C* 72.1 (July 2005). ISSN: 1089-490X. DOI: 10.1103/physrevc.72.014907. URL: http://dx.doi.org/10.1103/PhysRevC.72.014907.

[26] R. Walz, K. Boguslavski, and J. Berges. “Large- <mml:math xmlns:mml=”http://www.w3.org/1998/Math/M display=”inline”><mml:mi>N</mml:mi></mml:math> kinetic theory for highly occupied systems”. In: *Physical Review D* 97.11 (June 2018). ISSN: 2470-0029. DOI: 10.1103/physrevd.97.116011. URL: http://dx.doi.org/10.1103/PhysRevD.97.116011.

[27] Jürgen Berges and Julien Serreau. “Progress in nonequilibrium quantum field theory”. In: *Strong and Electroweak Matter 2002*. World Scientific, June 2003. DOI: 10.1142/9789812704498_0011. URL: http://dx.doi.org/10.1142/9789812704498_0011.

[28] J. Berges et al. “Lattice simulations of real-time quantum fields”. In: *Physical Review D* 75.4 (Feb. 2007). ISSN: 1550-2368. DOI: 10.1103/physrevd.75.045007. URL: http://dx.doi.org/10.1103/PhysRevD.75.045007.

[29] Jürgen Berges, Kirill Boguslavski, and Sören Schlichting. “Nonlinear amplification of instabilities with longitudinal expansion”. In: *Physical Review D* 85.7 (Apr. 2012). ISSN: 1550-2368. DOI: 10.1103/physrevd.85.076005. URL: http://dx.doi.org/10.1103/PhysRevD.85.076005.

[30] Peter B Arnold, Guy D Moore, and Laurence G Yaffe. “Effective kinetic theory for high temperature gauge theories”. In: *Journal of High Energy Physics* 2003.01 (Jan. 2003), pp. 030–030. ISSN: 1029-8479. DOI: 10.1088/1126-6708/2003/01/030. URL: http://dx.doi.org/10.1088/1126-6708/2003/01/030.

[31] Ralf-Arno Tripolt et al. *Finite-Temperature Spectral Functions from the Functional Renormalization Group*. 2013. arXiv: 1311.4304 [hep-lat].

[32] R.-A. Tripolt, L. von Smekal, and J. Wambach. “Spectral functions and in-medium properties of hadrons”. In: *International Journal of Modern Physics E* 26.01n02 (Jan. 2017), p. 1740028. ISSN: 1793-6608. DOI: 10.1142/s0218301317400286. URL: http://dx.doi.org/10.1142/S0218301317400286.

[33] Kazuhiko Kamikado et al. “Real-time correlation functions in the $O(N)$ model from the functional renormalization group”. In: *The European Physical Journal C* 74.3 (Mar. 2014). ISSN: 1434-6052. DOI: 10.1140/epjc/s10052-014-2806-6. URL: http://dx.doi.org/10.1140/epjc/s10052-014-2806-6.

[34] S. Huelsmann, S. Schlichting, and P. Scior. “Spectral functions from the real-time functional renormalization group”. In: *Physical Review D* 102.9 (Nov. 2020). ISSN: 2470-0029. DOI: 10.1103/physrevd.102.096004. URL: http://dx.doi.org/10.1103/PhysRevD.102.096004.

[35] Jürgen Berges and Thomas Gasenzer. “Quantum versus classical statistical dynamics of an ultracold Bose gas”. In: *Physical Review A* 76.3 (Sept. 2007). ISSN: 1094-1622. DOI: 10.1103/physreva.76.033604. URL: http://dx.doi.org/10.1103/PhysRevA.76.033604.

[36] Andreas Schachner, Asier Piñeiro Orioli, and Jürgen Berges. “Universal scaling of unequal-time correlation functions in ultracold Bose gases far from equilibrium”. In: *Physical Review A* 95.5 (May 2017). ISSN: 2469-9934. DOI: 10.1103/physreva.95.053605. URL: http://dx.doi.org/10.1103/PhysRevA.95.053605.

[37] Asier Piñeiro Orioli, Kirill Boguslavski, and Jürgen Berges. “Universal self-similar dynamics of relativistic and nonrelativistic field theories near nonthermal fixed points”. In: *Physical Review D* 92.2 (July 2015). ISSN: 1550-2368. DOI: 10.1103/physrevd.92.025041. URL: http://dx.doi.org/10.1103/PhysRevD.92.025041.

[38] Christian-Marcel Schmied, Aleksandr N. Mikheev, and Thomas Gasenzer. “Prescaling in a Far-from-Equilibrium Bose Gas”. In: *Physical Review Letters* 122.17 (May 2019). ISSN: 1079-7114. DOI: 10.1103/physrevlett.122.170404. URL: http://dx.doi.org/10.1103/PhysRevLett.122.170404.

[39] Kirill Boguslavski, Tuomas Lappi, and Sören Schlichting. “Fermion and gluon spectral functions far from equilibrium”. In: *EPJ Web of Conferences* 258 (2022). Ed. by A. Rothkopf et al., p. 05003. ISSN: 2100-014X. DOI: 10.1051/epjconf/202225805003. URL: http://dx.doi.org/10.1051/epjconf/202225805003.

[40] Harshit Pandey, Soeren Schlichting, and Sayantan Sharma. *Heavy quark momentum broadening in a non-Abelian plasma away from thermal equilibrium*. 2023. arXiv: 2312.12280 [hep-lat].

[41] Jürgen Berges, Sören Schlichting, and Dénes Sexty. “Dynamic critical phenomena from spectral functions on the lattice”. In: *Nuclear Physics B* 832.1–2 (June 2010), pp. 228–240. ISSN: 0550-3213. DOI: 10.1016/j.nuclphysb.2010.02.007. URL: http://dx.doi.org/10.1016/j.nuclphysb.2010.02.007.

[42] Thimo Preis, Michal P. Heller, and Jürgen Berges. “Stable and Unstable Perturbations in Universal Scaling Phenomena Far from Equilibrium”. In: *Physical Review Letters* 130.3 (Jan. 2023). ISSN: 1079-7114. DOI: 10.1103/physrevlett.130.031602. URL: http://dx.doi.org/10.1103/PhysRevLett.130.031602.

[43] Gert Aarts and Anders Tranberg. "Nonequilibrium dynamics in the $O(N)$ model to next-to-next-to-leading order in the $1/N$ expansion". In: *Physical Review D* 74.2 (July 2006). ISSN: 1550-2368. DOI: 10.1103/physrevd.74.025004. URL: http://dx.doi.org/10.1103/PhysRevD.74.025004.

[44] Gert Aarts and Jürgen Berges. "Nonequilibrium time evolution of the spectral function in quantum field theory". In: *Physical Review D* 64.10 (Oct. 2001). ISSN: 1089-4918. DOI: 10.1103/physrevd.64.105010. URL: http://dx.doi.org/10.1103/PhysRevD.64.105010.

[45] Gert Aarts and Jan Smit. "Classical approximation for time dependent quantum field theory: Diagrammatic analysis for hot scalar fields". In: *Nucl. Phys. B* 511 (1998), pp. 451–478. DOI: 10.1016/S0550-3213(97)00723-2. arXiv: hep-ph/9707342.

[46] Johannes V. Roth et al. "Real-time methods for spectral functions". In: *Physical Review D* 105.11 (June 2022). ISSN: 2470-0029. DOI: 10.1103/physrevd.105.116017. URL: http://dx.doi.org/10.1103/PhysRevD.105.116017.

[47] Sören Schlichting, Dominik Smith, and Lorenz von Smekal. "Spectral functions and critical dynamics of the $O(4)$ model from classical-statistical lattice simulations". In: *Nuclear Physics B* 950 (Jan. 2020), p. 114868. ISSN: 0550-3213. DOI: 10.1016/j.nuclphysb.2019.114868. URL: http://dx.doi.org/10.1016/j.nuclphysb.2019.114868.

[48] Dominik Schweitzer, Sören Schlichting, and Lorenz von Smekal. "Spectral functions and dynamic critical behavior of relativistic Z_2 theories". In: *Nuclear Physics B* 960 (Nov. 2020), p. 115165. ISSN: 0550-3213. DOI: 10.1016/j.nuclphysb.2020.115165. URL: http://dx.doi.org/10.1016/j.nuclphysb.2020.115165.

[49] Sören Schlichting. "Turbulent thermalization of weakly coupled non-Abelian plasmas". In: *Physical Review D* 86.6 (Sept. 2012). ISSN: 1550-2368. DOI: 10.1103/physrevd.86.065008. URL: http://dx.doi.org/10.1103/PhysRevD.86.065008.

[50] S. Yu. Khlebnikov and I. I. Tkachev. "Classical Decay of the Inflaton". In: *Physical Review Letters* 77.2 (July 1996), pp. 219–222. ISSN: 1079-7114. DOI: 10.1103/physrevlett.77.219. URL: http://dx.doi.org/10.1103/PhysRevLett.77.219.

[51] J. Berges. *Nonequilibrium Quantum Fields: From Cold Atoms to Cosmology*. 2015. arXiv: 1503.02907 [hep-ph].

[52] J. von Neumann. “Wahrscheinlichkeitstheoretischer Aufbau der Quantenmechanik”. In: *Nachrichten von der Gesellschaft der Wissenschaften zu Göttingen, Mathematisch-Physikalische Klasse* 1927 (1927), pp. 245–272. URL: http://eudml.org/doc/59230.

[53] Mikko Laine and Aleksi Vuorinen. *Basics of Thermal Field Theory*. Springer International Publishing, 2016. DOI: 10.1007/978-3-319-31933-9. URL: https://doi.org/10.1007%2F978-3-319-31933-9.

[54] Mark Srednicki. *Quantum Field Theory: Spin Zero*. 2004. arXiv: hep-th/0409035 [hep-th].

[55] Robert M Wald. *General relativity*. Chicago, IL: Chicago Univ. Press, 1984.

[56] Kevin Dusling, François Gelis, and Raju Venugopalan. “The initial spectrum of fluctuations in the little bang”. In: *Nuclear Physics A* 872.1 (Dec. 2011), pp. 161–195. DOI: 10.1016/j.nuclphysa.2011.09.012. URL: https://doi.org/10.1016%2Fj.nuclphysa.2011.09.012.

[57] R. F. O’Connell. *The Wigner Distribution*. 2010. arXiv: 1009.4431 [quant-ph].

[58] K. Boguslavski et al. “Spectral function for overoccupied gluodynamics from real-time lattice simulations”. In: *Physical Review D* 98.1 (July 2018). DOI: 10.1103/physrevd.98.014006. URL: https://doi.org/10.1103%2Fphysrevd.98.014006.

[59] Kirill Boguslavski and Asier Piñeiro Orioli. “Unraveling the nature of universal dynamics in $O(N)$ theories”. In: *Physical Review D* 101.9 (May 2020). ISSN: 2470-0029. DOI: 10.1103/physrevd.101.091902. URL: http://dx.doi.org/10.1103/PhysRevD.101.091902.

[60] Aleksandr N. Mikheev, Ido Siovitz, and Thomas Gasenzer. *Universal dynamics and non-thermal fixed points in quantum fluids far from equilibrium*. 2023. arXiv: 2304.12464 [cond-mat.quant-gas].

[61] Kirill Boguslavski. “Universality classes far from equilibrium: From heavy-ion collisions to superfluid Bose systems”. PhD thesis. U. Heidelberg, ITP, May 2016. DOI: 10.11588/heidok.00021780.

[62] Asier Piñeiro Orioli and Jürgen Berges. “Breaking the Fluctuation-Dissipation Relation by Universal Transport Processes”. In: *Physical Review Letters* 122.15 (Apr. 2019). DOI: 10.1103/physrevlett.122.150401. URL: https://doi.org/10.1103%2Fphysrevlett.122.150401.

[63] A. Kurkela, T. Lappi, and J. Peuron. “Time evolution of linearized gauge field fluctuations on a real-time lattice”. In: *The European Physical Journal C* 76.12 (Dec. 2016). ISSN: 1434-6052. DOI: 10.1140/epjc/s10052-016-4523-9. URL: http://dx.doi.org/10.1140/epjc/s10052-016-4523-9.

[64] Matteo Frigo and Steven G. Johnson. “The Design and Implementation of FFTW3”. In: *Proceedings of the IEEE* 93.2 (2005). Special issue on “Program Generation, Optimization, and Platform Adaptation”, pp. 216–231.